Title

Spatial and temporal variations of aerosols around Beijing in summer 2006: Model evaluation and source apportionment

Journal

Journal of Geophysical Research Atmospheres, 114(15)

ISSN

0148-0227

Authors

Matsui, H
Koike, M
Kondo, Y
et al.

Publication Date

2009-08-16

DOI

10.1029/2008JD010906

Spatial and temporal variations of aerosols around Beijing in summer 2006: Model evaluation and source apportionment

H. Matsui,[1,2] M. Koike,[1] Y. Kondo,[3] N. Takegawa,[3] K. Kita,[4] Y. Miyazaki,[3,5] M. Hu,[6] S.-Y. Chang,[7] D. R. Blake,[8] J. D. Fast,[9] R. A. Zaveri,[9] D. G. Streets,[10] Q. Zhang,[10] and T. Zhu[6]

Received 31 July 2008; revised 6 May 2009; accepted 12 May 2009; published 15 August 2009.

[1] Regional aerosol model calculations were made using the Weather Research and Forecasting (WRF)-Community Multiscale Air Quality (CMAQ) and WRF-chem models to study spatial and temporal variations of aerosols around Beijing, China, in the summer of 2006, when the Campaigns of Air Quality Research in Beijing and Surrounding Region 2006 (CAREBeijing) intensive campaign was conducted. Model calculations captured temporal variations of primary (such as elemental carbon (EC)) and secondary (such as sulfate) aerosols observed in and around Beijing. The spatial distributions of aerosol optical depth observed by the MODIS satellite sensors were also reproduced over northeast China. Model calculations showed distinct differences in spatial distributions between primary and secondary aerosols in association with synoptic-scale meteorology. Secondary aerosols increased in air around Beijing on a scale of about 1000 $\times$ 1000 km^2 under an anticyclonic pressure system. This air mass was transported northward from the high anthropogenic emission area extending south of Beijing with continuous photochemical production. Subsequent cold front passage brought clean air from the north, and polluted air around Beijing was swept to the south of Beijing. This cycle was repeated about once a week and was found to be responsible for observed enhancements/reductions of aerosols at the intensive measurement sites. In contrast to secondary aerosols, the spatial distributions of primary aerosols (EC) reflected those of emissions, resulting in only slight variability despite the changes in synoptic-scale meteorology. In accordance with these results, source apportionment simulations revealed that primary aerosols around Beijing were controlled by emissions within 100 km around Beijing within the preceding 24 h, while emissions as far as 500 km and within the preceding 3 days were found to affect secondary aerosols.

Citation: Matsui, H., et al. (2009), Spatial and temporal variations of aerosols around Beijing in summer 2006: Model evaluation and source apportionment, *J. Geophys. Res.*, *114*, D00G13, doi:10.1029/2008JD010906.

1. Introduction

[2] In East Asia, recent rapid growth of industrial activity has been causing a large increase in emissions of pollutants such as aerosols and their precursor gases. The increase in aerosols in the atmosphere potentially has significant impacts on regional climate and air quality. Recently, megacities have attracted considerable attention owing to their large emissions, which can also cause regional-scale impacts. It is therefore critical to understand the key chemical and transport processes that control aerosol concentrations in and around megacities.

[3] Beijing, the capital of China, is one of the largest megacities in Asia. *Chan and Yao* [2008] recently reviewed air pollution in megacity regions in China, including Beijing. The annual average concentration of particulate matter smaller than 2.5 μm in diameter ($PM_{2.5}$) was reported to be about 100 μg m^{-3}, which is far greater than the WHO Air Quality Guideline [*World Health Organization*, 2006]. Several recent modeling studies indicated the importance of

[1]Department of Earth and Planetary Science, Graduate School of Science, University of Tokyo, Tokyo, Japan.
[2]Now at Research Center for Advanced Science and Technology, University of Tokyo, Tokyo, Japan.
[3]Research Center for Advanced Science and Technology, University of Tokyo, Tokyo, Japan.
[4]Department of Environmental Science, Graduate School of Science, Ibaraki University, Mito, Japan.
[5]Now at Institute of Low Temperature Science, Hokkaido University, Sapporo, Japan.
[6]State Key Laboratory of Environmental Simulation and Pollution Control, College of Environmental Sciences, Peking University, Beijing, China.
[7]Department of Public Health, Chung Shan Medical University, Taichung City, Taiwan.
[8]Department of Chemistry, University of California, Irvine, California, USA.
[9]Atmospheric Science and Global Change Division, Pacific Northwest National Laboratory, Richland, Washington, USA.
[10]Decision and Information Sciences Division, Argonne National Laboratory, Argonne, Illinois, USA.

0148-0227/09/2008JD010906

emissions outside of Beijing to aerosol levels in Beijing. *An et al.* [2007] calculated $PM_{2.5}$ and PM_{10} concentrations around Beijing using the Community Multiscale Air Quality (CMAQ) model, and compared modeling results with measured PM concentrations and aerosol optical depth (AOD) during a high concentration episode in April 2005. They reported that the percentage contribution of non-Beijing sources was about 39 and 15% in the northwest and southwest regions of urban Beijing. *Streets et al.* [2007] conducted regional model simulations over the Beijing region in July 2001 using the CMAQ model. They showed that about 34% of $PM_{2.5}$ and 35–60% of ozone (O_3) during high O_3 episodes at the Beijing Olympic Stadium site in summer could be attributed to sources outside Beijing. They also showed that Hebei Province, which is located to the south of Beijing, could contribute 50–70% of $PM_{2.5}$ and 20–30% of O_3 concentrations in Beijing. *Chen et al.* [2007] also estimated the contribution from outside Beijing in 2002 by changing emissions in surrounding provinces. They showed that, on annual average, 35% of PM_{10} came from sources outside Beijing. These studies suggested the importance of a regional-scale viewpoint to understand aerosol concentrations in Beijing. However, systematic analyses on behaviors of regional-scale aerosol concentrations around Beijing have not been made in association with the aerosol/precursor source distributions, meteorological fields, transport processes, and photochemical production of secondary aerosols. Furthermore, these previous studies examined only total PM concentrations and did not discuss individual aerosol compounds.

[4] The Campaigns of Air Quality Research in Beijing and Surrounding Region 2006 (CAREBeijing-2006) campaign was conducted in August and September 2006 in and around Beijing. Two intensive sites were deployed for this campaign: the Peking University (PKU) site is an urban site located on the Peking University campus (39.99°N, 116.31°E), in Beijing, and the Yufa site is a suburban site (39.51°N, 116.31°E) on the campus of Huang Pu Military College, which is located about 50 km south of Beijing. A major goal of this campaign is to make contributions to the systematic understanding of the behaviors of aerosol and gaseous species in the Beijing region. In this study, spatial and temporal variations of gaseous and aerosol species around Beijing are simulated for the period of the CAREBeijing-2006 campaign using a regional three-dimensional model, Weather Research and Forecasting (WRF)-CMAQ. Model calculations are compared in detail with in situ measurements made at the PKU and Yufa sites to evaluate its performance. In addition, comparison is made with Moderate Resolution Imaging Spectroradiometer (MODIS) satellite measurements of AOD to evaluate model performance in simulating regional-scale aerosol distributions. Following these evaluation studies, we utilize model calculations to interpret temporal variations of aerosols at two intensive sites from the viewpoint of regional-scale aerosol distributions affected by synoptic-scale meteorology. Contributions of emissions in various locations to aerosol concentrations in Beijing are evaluated by changing emissions in individual locations. The characteristic time for accumulation of aerosols in the atmosphere is also estimated for primary (EC) and secondary (sulfate) aerosols.

[5] In order to quantify uncertainties in the model predictions, model calculations are conducted using another regional three-dimensional model, WRF-chem. These calculations are compared with WRF-CMAQ calculations and observations. Note that this study does not aim to describe reasons for the differences between model predictions but shows ranges of simulation results. Because the WRF-chem model has recently been developed [*Grell et al.*, 2005; *Fast et al.*, 2006] and evaluation studies have been made for only limited case studies [*McKeen et al.*, 2005, 2007; *Fast et al.*, 2006; *Gustafson et al.*, 2007], we intend to contribute to model validation by applying it to a megacity in Asia.

[6] In sections 2 and 3, measurements and regional three-dimensional models used in this study, respectively, are described. In section 4, results of WRF-CMAQ calculations are shown and compared with observations at intensive sites (the PKU and Yufa sites). In section 5, comparison with MODIS measurements is shown. In section 6, temporal variations of regional-scale aerosol distributions are presented in order to interpret temporal variations of aerosol mass concentrations observed at the intensive sites. In section 7, spatial and temporal source apportionments are discussed by presenting results of sensitivity simulations. In section 8, WRF-chem simulations are compared with WRF-CMAQ simulations and observations. In section 9, a summary of this paper is given.

2. Measurements

[7] Table 1 shows a list of the measurements that were used in this study to evaluate the model performance at the PKU and Yufa sites between 10 August and 11 September 2006. Details of the observation sites and measurements are found in other CAREBeijing-2006 papers [*Takegawa et al.*, 2009b; *Garland et al.*, 2009]. At the Yufa site, inorganic aerosol mass concentrations, such as sulfate (SO_4^{2-}), nitrate (NO_3^-), and ammonium (NH_4^+), in PM_1 particles (50% cutoff at a vacuum aerodynamic diameter of 1 μm) were measured using an Aerodyne Aerosol Mass Spectrometer (AMS) [*Takegawa et al.*, 2009b]. AMS measurements of SO_4^{2-} and NH_4^+ agreed with Berner impactor measurements to 15%, while AMS NO_3^- values were smaller by 40%, likely owing to a difference in the size cut between the two measurements [*Takegawa et al.*, 2009a]. At the PKU site, inorganic aerosol mass concentrations of PM_{10} particles were measured using a PILS-type instrument. Mass concentrations of PM_1 elemental and organic carbon (EC and OC) were measured using a Sunset Laboratory semicontinuous EC/OC analyzer with a thermal optical method both at the PKU and Yufa sites. In this study, we estimated primary and secondary OC (POC and SOC) by assuming constant POC/EC ratios, following the idea proposed by *Turpin and Huntzicker* [1995]. Total $PM_{2.5}$ mass concentration was measured by a Tapered Element Oscillating Microbalance (TEOM). Concentrations of gaseous species, such as carbon monoxide (CO), NO_x (= NO + NO_2), ozone (O_3), and sulfur dioxide (SO_2), were measured at both the PKU and Yufa sites [*Takegawa et al.*, 2006; *Kondo et al.*, 2008]. In addition, volatile organic compounds (VOCs) were measured by whole air sampling followed by analyses using a multicolumn GC-FID/ECD/MS system at the University of California, Irvine [*Colman et al.*, 2001]. In total, 16 and 87 samples were collected at the PKU and Yufa sites, respectively. Meteorological components such as tempera-

Table 1. CAREBeijing-2006 Data Sets Used in This Study

Species/Parameter	Site	Instrument	PI	Reference
Meteorology	PKU[a]	LASTEM	M. Hu (PKU)	–
CO	PKU	EC9830	M. Hu (PKU)	–
NO_x	PKU	EC9841	M. Hu (PKU)	–
O_3	PKU	EC9810	M. Hu (PKU)	–
SO_2	PKU	EC9850	M. Hu (PKU)	–
VOCs	PKU	Canister/GC-FID etc.	D. R. Blake (UCI[b])	*Colman et al.* [2001]
Inorganics	PKU	PILS-type	S-Y Chang (CSMU[c])	*Chang et al.* [2007]
ECOC	PKU	Sunset ECOC	Y. Kondo (UT) M. Hu (PKU)	*Kondo et al.* [2006]
Meteorology	Yufa[d]	LASTEM	M. Hu (PKU)	–
CO	Yufa	NDIR-TECO	Y. Kondo (UT[e])	*Takegawa et al.* [2006]
NO_x	Yufa	Photolysis Converter + TECO	Y. Kondo (UT)	*Kondo et al.* [2008]
O_3	Yufa	TECO	K. Kita (IU[f])	*Kondo et al.* [2008]
SO_2	Yufa	ML9850B	M. Hu (PKU)	–
VOCs	Yufa	Canister/GC-FID etc.	D. R. Blake (UCI)	*Colman et al.* [2001]
Inorganics	Yufa	Aerodyne AMS	N. Takegawa (UT)	*Takegawa et al.* [2009a]
ECOC	Yufa	Sunset ECOC	Y. Kondo (UT) M. Hu (PKU)	*Kondo et al.* [2006]
$PM_{2.5}$	Yufa	TEOM	M. Hu (PKU)	–

[a]PKU stands for the Peking University, China. The PKU site is located at 39.99°N, 116.31°E.
[b]UCI stands for the University of California-Irvine, USA.
[c]CSMU stands for Chung Shan Medical University, Taiwan.
[d]The Yufa site is located at 39.51°N, 116.31°E.
[e]UT stands for the University of Tokyo, Japan.
[f]IU stands for Ibaraki University, Japan.

ture, wind speed and direction, and relative humidity were also measured at both sites.

[8] In addition to the CAREBeijing-2006 campaign, spatial distributions of model calculated AOD are also compared with satellite measurements made by MODIS [*Remer et al.*, 2005]. In this study, level 2 Terra and Aqua AOD data (MOD04_L2) are used.

3. Regional Three-Dimensional Model

3.1. General Description

[9] In this study, the WRF-CMAQ three-dimensional regional model was used. Although the WRF-chem model was also used in this study, a description of the model and its results are presented in section 8. WRF-CMAQ is an off-line model, in which the meteorological field is calculated first using the nonhydrostatic Weather Research and Forecasting (WRF) model version 2.2 with advanced research WRF core [*Skamarock et al.*, 2005]. The chemical field is consecutively calculated using the Model-3/Community Multiscale Air Quality (CMAQ) model version 4.6 developed by the U.S. EPA [*Byun and Ching*, 1999; *Binkowski and Roselle*, 2003] using the meteorological field calculated by WRF.

[10] The parameterization schemes and options of the WRF-CMAQ calculations are listed in Table 2. When WRF meteorological calculations were made, analysis nudging was applied every 6 h using National Centers for Environmental Prediction (NCEP) global objective final analysis (FNL) data (1° × 1° and 19 layers up to 100 hPa) to calculate the horizontal wind field (u and v), temperature (T), and water vapor (q).

[11] Three domains (domains 1, 2, and 3 shown in Figure 1) were employed for WRF-CMAQ calculations. Domains 1, 2, and 3 contain 70 × 60, 48 × 48, and 54 × 54 grid cells, with horizontal resolutions of 81, 27, and 9 km, respectively. The center of domain 1 is 32°N and 105°E, while that of domains 2 and 3 is 40°N and 116°E, which corresponds to the location of Beijing. All domains have 18 vertical layers from the surface to 100 hPa, with finer vertical resolutions near the ground. The lowest layer is approximately 30 m in depth. Two-way nesting was conducted for WRF calculations, while one-way nesting was adopted for CMAQ calculations. The chemistry boundary conditions of domain 1 in the CMAQ calculations were chosen to be constant background values. Calculations were made for the period between 10 August and 11 September 2006. Unless indicated otherwise, model results at the PKU and Yufa sites are presented from domain 3, the highest spatial resolution grid.

3.2. CMAQ Model

[12] Because detailed descriptions of CMAQ can be found in the literature [*Byun and Ching*, 1999; *Binkowski and*

Table 2. Meteorological and Chemical Process Options Employed by WRF-CMAQ and WRF-chem in This Study

	Model Option	
Atmospheric Process	WRF-CMAQ	WRF-chem
	Meteorology	
Longwave radiation	RRTM	RRTM
Shortwave radiation	Goddard	Goddard
Surface layer	Monin-Obukhov	Monin-Obukhov
Land surface	Noah	Noah
Boundary layer	YSU	YSU
Cumulus clouds	Kain-Fritsch	Kain-Fritsch
Cloud microphysics	Lin et al.	Lin et al.
	Chemistry	
Gas phase chemistry	SAPRC99	CBM-Z
Aerosol processes	AERO3	MOSAIC
Gas/aerosol partitioning	ISORROPIA	ASTEM
Aerosol thermodynamics	ISORROPIA	MESA
Aqueous phase chemistry	RADM	*Fahey and Pandis* [2001]
Photolysis	JPROC/PHOT	Fast-J

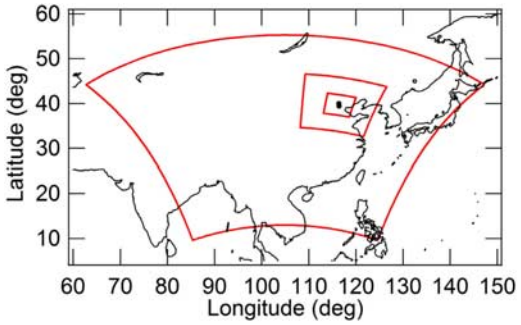

Figure 1. Three simulation domains employed in this study. Black circles show locations of the Peking University (PKU) and Yufa sites, where intensive measurements were made during the CAREBeijing-2006 campaign.

Roselle, 2003], only brief descriptions are given in this paper. As shown in Table 2, the SAPRC99 gas phase chemistry mechanism, which includes 84 lumped model species and 214 reactions [*Carter*, 2000], was used. Aerosol dynamics were simulated with the third generation CMAQ aerosol module (AERO3) [*Binkowski and Roselle*, 2003]. The aerosol size distributions are represented by a superposition of three lognormal distributions, namely the Aitken, accumulation, and coarse modes. The fine particle concentrations of SO_4^{2-}, NO_3^-, NH_4^+, primary and secondary organic aerosols (POA and SOA), other $PM_{2.5}$ (nonreactive dust), and aerosol water were predicted by calculating aerosol processes such as nucleation, coagulation, condensation, dry deposition, and cloud processes. Equilibrium between gases and accumulation mode aerosols was calculated with the ISORROPIA thermodynamic module version 1.7 [*Nenes et al.*, 1998]. In this study, MCIP version 3.2 was used for meteorology preprocessing.

3.3. Emissions

[13] Anthropogenic emission inventories were developed for the year 2004 with a horizontal resolution of 0.5 × 0.5 degrees. These emission inventories were developed by revising those reported by *Streets et al.* [2003, 2006, 2007], *Bond et al.* [2004], and *Zhang et al.* [2007] using the method described by *Zhang et al.* [2009]. Note that emissions for the years 2000, 2001, and 2006 were presented by *Zhang et al.* [2009], while those for the year 2004 are used in this study. Table 3 shows comparisons of emissions of carbon dioxide (CO_2), CO, NO_x, SO_2, EC, and OC used in this study and those reported by *Streets et al.* [2003]. For all species listed in Table 3, the emissions used in this study were greater than those reported by *Streets et al.* [2003] by a factor of 1.5 to 2.5, in both the Beijing area (defined as 39°–40°N and 116°–117°E) and domain 2 (33°–43°N and 111°–121°E), which covers the northeast part of China. These increases are attributed mostly to actual emissions growth since 2000, in addition to improvements in estimation methodology (e.g., a more detailed technology-based approach) [*Zhang et al.*, 2009]. *Zhang et al.* [2009] reported that the major causes of actual emissions growth in China are in the power plant sector and transportation. In Figure 2, annual emissions of anthropogenic CO, SO_2, and EC around Beijing as well as topography are shown. In Figure 2, black circles show the locations of the PKU and Yufa sites. Beijing is located on the northwest border of the Great North China Plain and is bordered by the Yanshan Mountains toward the north and west, which are higher than a thousand meters. Emissions are generally high along the Great North China Plain, which extends about 1000 km to the south of Beijing. Emissions from the Beijing area (39°–40°N and 116°–117°E) are especially large within the plain. In this study, hourly (maximum around noon and minimum during the night) and intraweek (reductions on weekends) dependencies of emissions were taken into account for individual emission sources (e.g., power plant, industry, residential, and transportation), while seasonal dependencies were not considered. It was also assumed that all of the emissions were emitted at the surface level (including power plant emissions) and that there were no emissions of primary particulate SO_4^{2-} and NO_3^-.

[14] Biogenic emission inventories developed as part of the Global Emissions Inventories Activity (GEIA) [*Guenther et al.*, 1995] were used in this study. These emission inventories contain monthly mean global emissions of isoprene and monoterpene for the year 1990 with a horizontal resolution of 1 × 1 degrees. In this study, average emissions in August and September were employed with simple hourly (maximum at noon and zero during the nighttime) dependencies. Dependencies on meteorological parameters (e.g., temperature, photosynthetically active radiation (PAR)) were not considered in this study.

[15] Before showing the various model results, scatterplots of concentrations at the PKU site between CO and several primary species, which are directly emitted into the atmosphere, are shown for observations and model calculations to examine the validity of emission data (Figure 3). The emission ratios between CO and individual compounds are also shown. For these plots, ΔCO and ΔCO_2 values were calculated by assuming background concentrations of these two species of 100 parts per billion by volume (ppbv) and 370 ppm by volume (ppmv), respectively, which are the minimum values observed during the CAREBeijing-2006 campaign. As can be seen in Figure 3, the ratios of model calculated concentrations are close to the emission ratios for all species shown here. The $\Delta CO/\Delta CO_2$ ratio showed reasonable agreement between observations and model calculations (Figure 3a), while model calculated $NO_x/\Delta CO$, SO_x (= SO_2 + SO_4^{2-})/ΔCO, EC/ΔCO, and POC/ΔCO ratios were systematically greater than observations by factors of 1.9, 4.1, 2.1, and 1.9, respectively (Figures 3b–3e). These results show that there are some inconsistencies in emission data among the species presented here, and the model calculations cannot agree with all of the observed species simultaneously. Although emissions for the whole of China were more accurately estimated by *Zhang et al.* [2009] as compared with previous studies, there can still be large uncertainties at individual locations. Systematically larger SO_2/CO emission ratios as compared with observations made in downtown Beijing were also reported in a previous study [*Li et al.*, 2007]. Considering that CO emissions from China for the year 2001 are in general agreement with aircraft measurements made during NASA's Transport and Chemical Evolution over the Pacific (TRACE-P) mission [*Streets et al.*, 2006], CO emissions used in this study may be reasonable on regional scales. Furthermore, as shown later in sections 4.1 and 8, both WRF-CMAQ and WRF-chem model

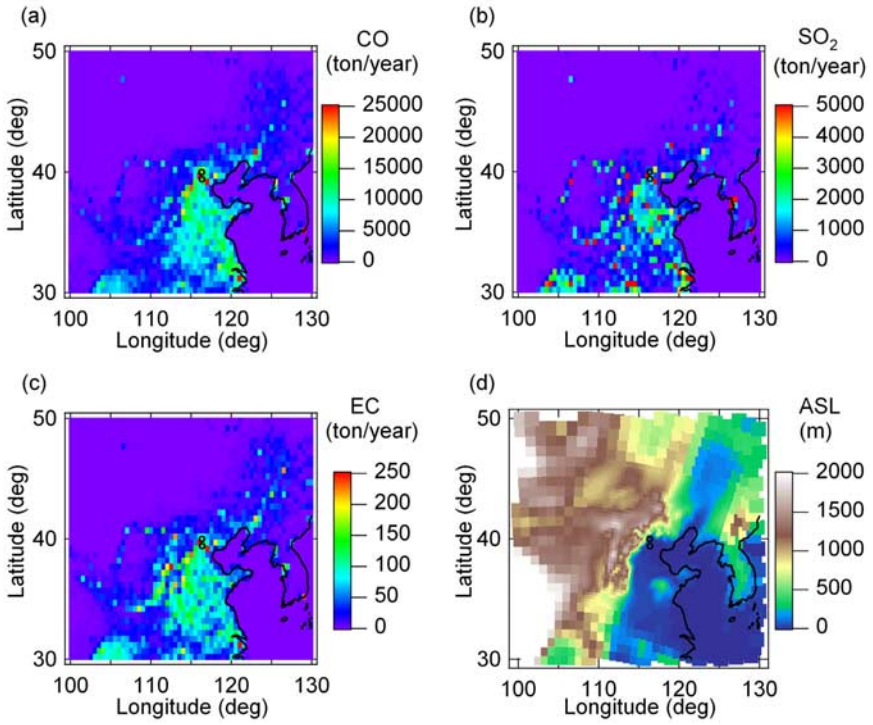

Figure 2. Emissions at surface level around Beijing for (a) CO, (b) SO_2, and (c) black carbon (BC, which is equivalent to elemental carbon (EC) in this paper). (d) Topography around Beijing. Black circles show the locations of the PKU and Yufa sites.

calculations reproduce observed CO concentrations well in this study, suggesting that emissions of NO_x, SO_2, EC, and POC may be overestimated at least around Beijing. However, the degrees of overestimation of these species (or underestimation of CO) can be different at individual locations because of the differences in the spatial distributions of emission sources. Consequently, it is difficult to scale emissions over the model domains using limited observations. Thus, we used the emission inventories without modification in this study, although some primary species are supposed to be overestimated in model calculations. In Appendix A1, results of model calculations are shown, in which emissions around Beijing were scaled so that emission ratios agree with observations.

[16] It is also noted that the PKU and Yufa sites are located within the same 0.5 × 0.5 degree emission grid cell. Because this grid cell covers a considerable part of Beijing, emissions in this grid cell can be too large for the Yufa area, considering the fact that the Yufa site is located in a suburban area. In fact, as shown in the following sections, mean positive biases of model calculated concentrations of primary species are systematically greater for the Yufa site as compared with those for the PKU site. Nevertheless, we compare model results with observations for individual sites rather than comparing averages, because the instrumentation and measurement techniques (e.g., size cut diameter of aerosol measurements) are different between the PKU and Yufa sites, as described in section 2.

4. Model Results and Comparison With Intensive Measurements

[17] Results of WRF-CMAQ calculations were compared with observations made at the PKU and Yufa sites to evaluate

Table 3. Emissions of Selected Species Reported by *Streets et al.* [2003] for the Year 2000 and Those Used in This Study for the Year 2004[a]

	Streets et al. [2003] (Year 2000)		This Study (Year 2004)	
Species	Domain 2 33°–43°N, 111°–121°E	Beijing 39°–40°N, 116°–117°E	Domain 2 33°–43°N, 111°–121°E	Beijing 39°–40°N, 116°–117°E
CO_2	8.79e+08	4.87e+07	1.68e+09	7.15e+07
CO	2.85e+07	1.24e+06	5.37e+07	1.74e+06
NO_x	2.51e+06	1.19e+05	5.16e+06	2.20e+05
SO_2	4.81e+06	2.36e+05	9.35e+06	2.62e+05
BC[b]	2.38e+05	8.01e+03	5.90e+05	1.77e+04
OC	6.03e+05	9.20e+03	8.85e+05	1.76e+04

[a]Unit is tons/year.
[b]BC (black carbon) is equivalent to EC (elemental carbon) in this study.

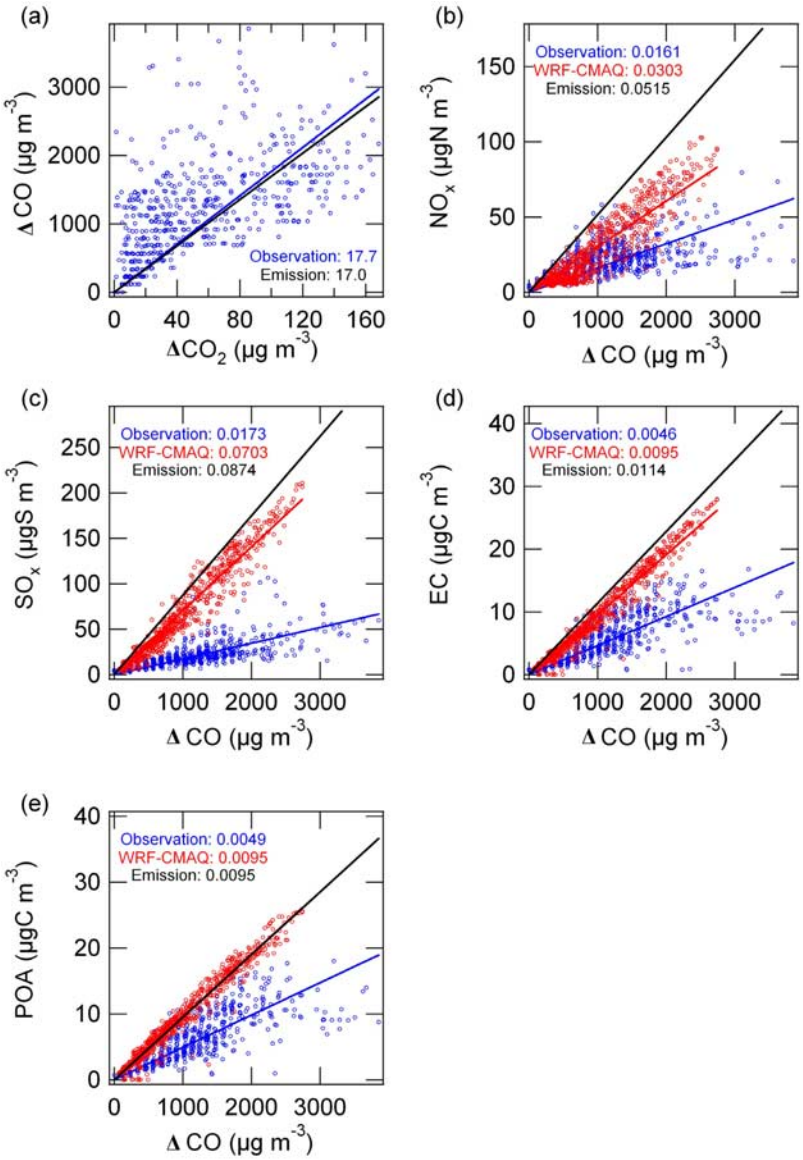

Figure 3. Scatterplots of concentrations at the PKU site between CO and several primary species, which are directly emitted into the atmosphere. Observations (blue) and WRF-CMAQ calculations (red) are shown for hourly data at the surface. The black line denotes the emission ratio in Beijing. The numerical value of the slope is also given.

the performance of model calculations. In Figures 4a–4i, comparisons at the Yufa site are shown for both meteorological and chemical parameters. The agreement between measurements and model calculations was evaluated using root mean square error (RMSE), mean bias (MB), normalized mean bias (NMB), and the correlation coefficient (R) (Appendix A2). These statistical analyses are made using all hourly data between 11 August and 10 September (31 days). The correlation coefficient was also calculated for daytime averages (0900–1600 LT) to evaluate the agreement of day-to-day variations. Results of these statistics at the PKU and Yufa sites are summarized in Table 4. WRF-chem model calculations and comparisons with WRF-CMAQ calculations are described in section 8.

4.1. Meteorological Fields

[18] In Figures 4a and 4b, model calculated wind speed and direction are compared with observations at the Yufa site. Meteorological conditions during the CAREBeijing-2006 campaign were characterized by stable atmospheric conditions under the influence of the Pacific high with occasional passages of migrating disturbances. Cold fronts or frontal zones passed over the PKU and Yufa sites in association with the migration of low-pressure systems several times, such as on 20 August and 3 and 8 September. On these occasions, the wind direction abruptly changed from southerly (180 degrees in Figure 4b) to northerly (0 or 360 degrees), and enhancements in wind speed were observed. Model calculations generally reproduced these observed variations of the wind

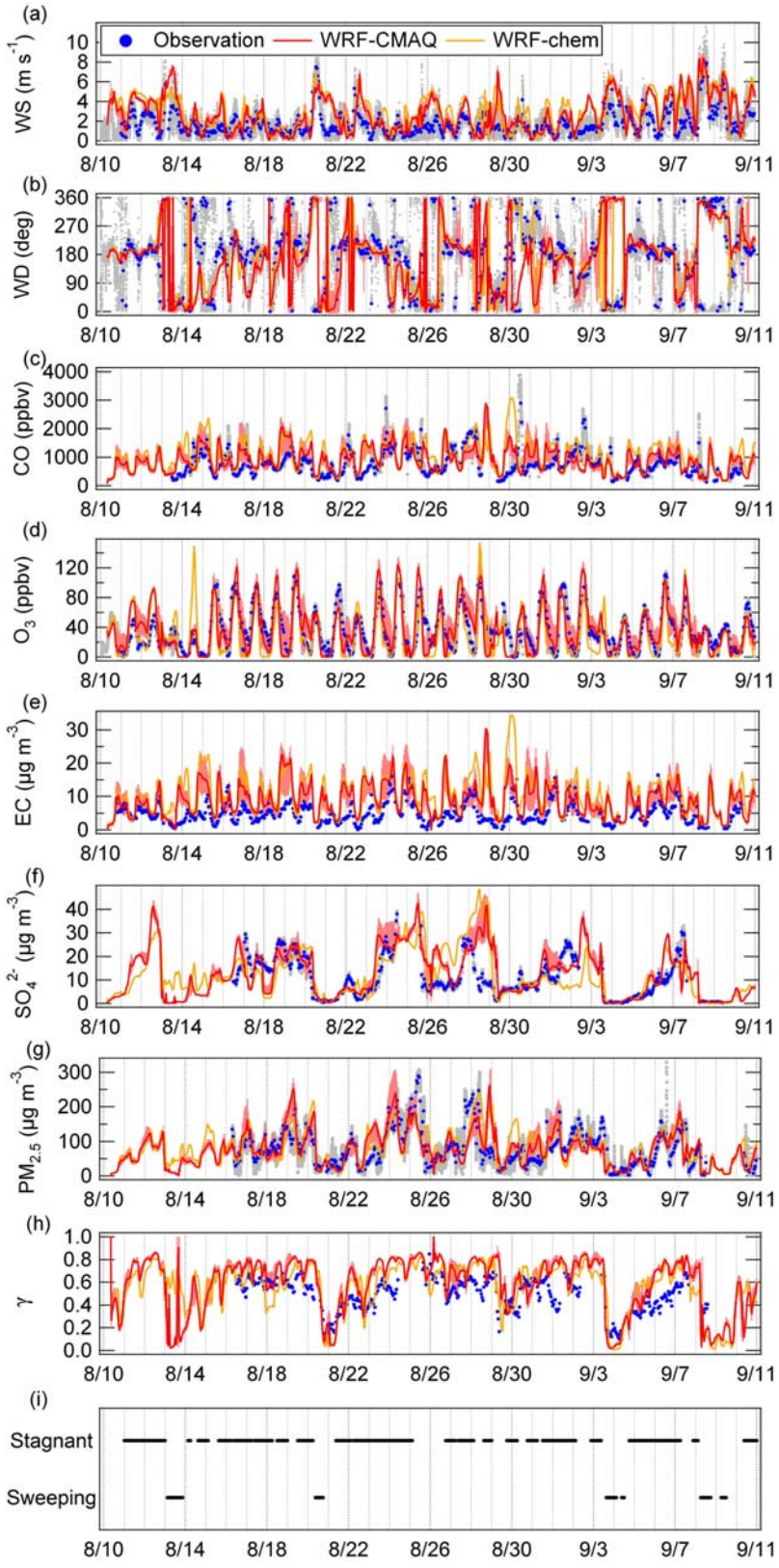
(a)
Observation
WRF-CMAQ
WRF-chem
WS (m s-1)
(b)
WD (deg)
(c)
CO (ppbv)
(d)
O3 (ppbv)
(e)
EC (μg m-3)
(f)
SO4 2- (μg m-3)
(g)
PM2.5 (μg m-3)
(h)
γ
(i)
Stagnant
Sweeping
8/10
8/14
8/18
8/22
8/26
8/30
9/3
9/7
9/11

Figure 4

Table 4. Evaluation Statistics on Meteorological and Chemical Components Calculated by WRF-CMAQ

Component	Units	Average		RMSE[a]	MB[a]	NMB[a] (%)	R[a]	
		Measured	Calculated				Hourly	Daily[b]
				PKU Site				
Temperature	K	299.0	299.2	2.16	0.25	0.084	0.89	0.87
Relative humidity	%	63.9	53.2	14.6	−10.7	−16.7	0.87	0.85
Wind speed	m s^{-1}	1.44	2.32	1.50	0.87	60.6	0.60	0.72
Wind speed (U)	m s^{-1}	0.47	0.55	–	–	–	0.41	0.76
Wind speed (V)	m s^{-1}	−0.026	0.029	–	–	–	0.54	0.65
CO	ppbv	1159	951	662	−208	−17.9	0.41	0.42
O_3	ppbv	28.8	48.8	33.7	20.0	69.5	0.81	0.74
NO_x	ppbv	38.5	48.1	36.2	9.57	24.9	0.53	0.44
SO_2	ppbv	8.62	47.6	53.5	39.0	452	0.069	0.24
Ethane	ppbv	2.95	2.36	1.29	−0.59	−20.0	0.58	0.53
Alkanes (C_3–C_8)	ppbv	17.0	12.0	13.7	−4.97	−29.2	0.60	0.48
Alkenes (C_2–C_5)	ppbv	6.55	6.64	4.42	0.095	1.45	−0.041	−0.17
Toluene	ppbv	3.93	1.40	3.62	−2.53	−64.4	0.72	0.48
Xylene	ppbv	1.74	0.73	1.46	−1.01	−58.3	0.36	0.12
Sulfate	μg m^{-3}	33.2	14.7	30.1	−18.5	−55.8	0.67	0.74
Ammonium	μg m^{-3}	20.5	14.6	16.3	−5.89	−28.7	0.38	0.60
Nitrate	μg m^{-3}	24.2	26.7	29.0	2.47	10.2	0.39	0.59
EC	μg m^{-3}	6.21	9.40	6.11	3.20	51.5	0.61	0.55
POC	μg m^{-3}	6.77	10.0	5.77	3.25	48.1	0.63	0.58
SOC	μg m^{-3}	4.43	0.92	4.59	−3.51	−79.2	0.40	0.75
				Yufa Site				
Temperature	K	297.3	298.1	2.24	0.81	0.27	0.91	0.87
Relative humidity	%	68.7	59.3	14.6	−9.40	−13.7	0.81	0.76
Wind speed	m s^{-1}	1.77	2.69	1.75	0.92	51.8	0.58	0.68
Wind speed (U)	m s^{-1}	0.15	−0.019	–	–	–	0.33	0.64
Wind speed (V)	m s^{-1}	0.59	0.032	–	–	–	0.58	0.86
CO	ppbv	771	962	522	191	24.7	0.31	0.51
O_3	ppbv	36.1	36.6	19.5	0.48	1.32	0.79	0.64
NO_x	ppbv	15.0	56.2	54.5	41.2	275	0.23	0.059
SO_2	ppbv	7.16	48.2	50.5	41.0	573	−0.15	0.33
Ethane	ppbv	4.65	1.94	5.67	−2.71	−58.3	0.48	0.54
Alkanes (C_3–C_8)	ppbv	10.5	8.90	14.4	−1.61	−15.3	0.36	0.45
Alkenes (C_2–C_5)	ppbv	3.65	4.16	4.14	0.50	13.8	0.33	0.34
Toluene	ppbv	3.38	0.86	10.1	−2.52	−74.6	−0.038	0.16
Xylene	ppbv	2.26	0.59	12.1	−1.67	−73.9	−0.079	0.28
Sulfate	μg m^{-3}	10.8	12.7	7.85	1.92	17.8	0.62	0.74
Ammonium	μg m^{-3}	4.74	10.9	9.33	6.13	129	0.64	0.74
Nitrate	μg m^{-3}	3.97	21.0	26.7	17.1	429	0.65	0.74
EC	μg m^{-3}	4.89	9.56	6.56	4.66	95.4	0.40	0.58
POC	μg m^{-3}	3.91	9.93	7.26	6.01	154	0.49	0.59
SOC	μg m^{-3}	2.43	0.88	2.71	−1.55	−63.8	0.32	0.50
$PM_{2.5}$	μg m^{-3}	80.9	86.7	46.1	5.76	7.12	0.62	0.76

[a]Definitions are given by equations (A1)–(A4) in Appendix A2.
[b]The correlation coefficient is calculated for daytime averages (0900–1600 LT).

field well. Although the absolute values of wind speed were overestimated by 50 to 60%, day-to-day wind variations were well reproduced at both sites (R = 0.64 − 0.86 for daytime averages, Table 4). Temperature and relative humidity were also generally reproduced well by model calculations (small RMSE and NMB, and large R), although relative humidity was slightly underestimated (NMB is −14 to −17%).

[19] Because of the distinct differences in meteorological conditions before and after the passage of cold fronts described above, the observation period was classified into three meteorological regimes based on wind speed and direction. The first one is the ''stagnant'' regime, in which the wind speed was less than 4 m s^{-1} and the wind direction was between 135° and 225° (from southeasterly to southwesterly). This regime appeared when the Beijing area was under the influence of a high-pressure system. The second, ''sweeping'' regime, is characterized by wind speeds greater than 4 m s^{-1} and wind direction between 315° and 45°

Figure 4. Time series of measurements (blue and gray circles for hourly average and high-frequency data, respectively) and model calculations (red and orange lines for the WRF-CMAQ and WRF-chem models, respectively) at the Yufa site. Red shading denotes the range of calculated values within 3 grid cells (27 × 27 km^2) for the WRF-CMAQ model around the Yufa site. (a) WS and (b) WD stand for the wind speed and wind direction, respectively. (c–d) Gas mixing ratios of CO and O_3. (e–g) Aerosol mass concentrations of EC, sulfate, and $PM_{2.5}$. (h) Index γ denotes secondary aerosols fraction defined by equation (1). (i) Definitions of air regime (stagnant or sweeping) are given in section 4.1. Results from the lowest model layer (midlevel altitude is about 16 m) are shown for model calculations. Dotted vertical lines denote every 0000 LT.

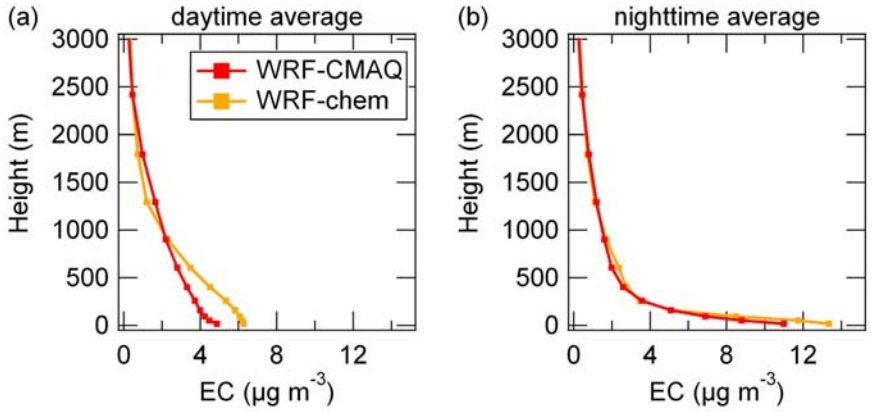

Figure 5. Vertical profiles of model calculated EC for daytime (0900–1600 LT) and nighttime (2100–0400 LT) averages at the Yufa site. Red and orange lines denote WRF-CMAQ and WRF-chem calculations, respectively.

(from northwesterly to northeasterly). This regime appeared for about 1 day upon passage of a cold front and brought clean air from the north. The last regime is for the remainder of the period. The time periods of these three regimes are shown in Figure 4i.

4.2. Chemical Fields

[20] In Figures 4c–4g, observed and model calculated (WRF-CMAQ) concentrations of CO, O_3, EC (fine particles), SO_4^{2-} (fine particles), and dry $PM_{2.5}$ aerosols are shown at the Yufa site. The CO concentration levels were generally reproduced at both sites, while EC concentrations were overestimated by 50 to 100% (Table 4). Systematic differences between the two species were caused by inconsistency in the emission data, as described in section 3.3. The overestimation of EC concentrations at Yufa was also caused by the limited spatial resolution of emission data (section 3.3).

[21] Observed EC concentrations show a clear diurnal variation, with a maximum at midnight to early morning superimposed on a moderate day-to-day variation (Figure 4e). A similar but less clear diurnal variation is also seen for CO (Figure 4c). In general, the model calculations successfully reproduced these variations. Analyses in vertical profiles of EC concentrations show that increases in model calculated concentrations during the night were due to accumulation of pollutants in association with lower planetary boundary layer height (Figures 5a and 5b). Diurnal variation of the emissions could also contribute to modify the diurnal variations of concentrations in the real atmosphere. The observed CO and EC concentrations also show moderate day-to-day variations, in which higher concentrations appeared in the ''stagnant'' regime. Model calculations captured these features to some extent (R values for daily averages were between 0.42 and 0.58, as shown in Table 4).

[22] As shown in Figure 4d, the observed O_3 concentration shows a distinct diurnal variation with a maximum in the early afternoon (1200 to 1500 LT), which was reproduced well by model calculations (R was 0.8 at both sites). Day-to-day variations were also generally well reproduced by model calculations, although the absolute concentrations were overestimated at the PKU site (NMB is 70%). The NO_x concentrations were overestimated by 30 and 280% at the PKU and Yufa sites, respectively. These results are again compatible with an inconsistency in emission data between species and the systematically large emissions for the Yufa area described in section 3.3. Alkanes (C_2–C_8) and aromatics were underestimated by 20–60% and 60–80%, respectively, while alkenes (C_2–C_5) agreed with observation to within 20% (Table 4).

[23] SO_2 concentrations were overestimated by factors of 5 and 6 at the PKU and Yufa sites, respectively (Table 4). Because the total sulfur ($SO_x = SO_2 + SO_4^{2-}$) concentrations were overestimated by roughly the same extent, the SO_2 overestimations were quite likely due to overestimations in SO_2 emissions around Beijing. Underestimation of the SO_2 oxidation rate and/or SO_2 dry deposition rate could also contribute to the SO_2 overestimation to some extent. One may consider that the overestimation in SO_2 emissions may result in an overestimation in SO_4^{2-} concentration in Beijing. To examine this point, we conducted sensitivity simulations with reduced SO_2 emissions so that model calculated SO_x/CO ratios agreed with observations at both the PKU and Yufa sites reasonably well, as described in Appendix A1. Results suggest that the reduction of SO_2 emissions near Beijing (within 150 km) does not affect sulfate concentrations in Beijing significantly. This is because sulfate concentrations are controlled by SO_2 emissions as far as 500 km from Beijing due to continuous oxidation during transport, as described in more detail in section 7.

[24] Model calculated mass concentrations of SO_4^{2-}, NO_3^-, and NH_4^+ in fine particles ($PM_{2.5}$) are compared with observations in Figure 4f and Table 4. As described in section 2, PM_{10} and PM_1 mass concentrations were observed at the PKU and Yufa sites, respectively, and therefore mass concentrations within different size ranges are compared here. However, it is suggested from the size-resolved chemical compositions derived from AMS and Berner impactor measurements that mass concentrations of PM_1 and $PM_{2.5}$ were not significantly different, at least for SO_4^{2-} and NH_4^+ [*Takegawa et al.*, 2009a]. The PM_{10} NO_3^- concentrations can be systematically greater than $PM_{2.5}$ NO_3^- concentrations. SO_4^{2-} concentrations were in good agreement at the Yufa site (NMB is 20%), while they were significantly underestimated

at the PKU site (NMB is −60%). Overestimations by 100 and 400% were found for NH_4^+ and NO_3^- concentrations at the Yufa site, while underestimation by 30% for NH_4^+ and good agreement for NO_3^- (NMB is 10%) were found at the PKU site. The overestimation of NO_3^- at the Yufa site mainly resulted from an overestimation of NO_x concentrations leading to too much HNO_3 formation in daytime.

[25] The features of day-to-day variations of SO_4^{2-}, NO_3^-, and NH_4^+ were generally reproduced well by the model calculations at both sites (the R values for daily averages were 0.59–0.74, as shown in Table 4). Enhancements of these species were observed at both sites 5 times during the 25-day observation period, suggesting regional phenomena extending at least 50 km, the distance between the two sites. This is consistent with small spatial variability in model calculated values (red shading in Figure 4f). These temporal variations in inorganic aerosol concentrations have a clear correspondence with the meteorological field, namely high concentrations appeared during the stagnant regime, while an abrupt decrease was observed in the sweeping regime [*Takegawa et al.*, 2009b]. Further discussion is given in section 6 from the viewpoint of the regional-scale distribution of aerosols under the synoptic-scale meteorological conditions during the campaign. It is noted that the diurnal variation is evident in addition to the day-to-day variation of primary aerosols (e.g., EC), while day-to-day variation is far more clearly seen with no clear diurnal variation of secondary aerosols (e.g., inorganic species). This contrast was captured well by the model calculations. The factors controlling this contrast are discussed in section 7.

[26] When model calculated POC concentrations are compared with those estimated from EC/OC measurements (section 2), model calculations are greater by 50 and 150% at the PKU and Yufa sites, respectively. The model calculation significantly underestimated SOC values and it accounted for only 20–30% of observed values at both sites. In the CMAQ aerosol module, SOA formation processes are formulated using an empirical representation based on results of chamber experiments such as *Odum et al.* [1996] and *Griffin et al.* [1999]. Similar severe underestimations of SOA concentrations in urban air were reported by previous studies [*Volkamer et al.*, 2006; *Matsui et al.*, 2009].

[27] Model calculated $PM_{2.5}$ dry mass concentrations are compared with observations in Figure 4g. Temporal variations of $PM_{2.5}$ show both diurnal and day-to-day variations, which likely resulted from diurnal variations of primary aerosols and day-to-day variations of secondary aerosols. Model calculations generally reproduced well these features of temporal variations as well as absolute concentrations.

[28] Finally, an index of secondary aerosol fraction within fine particles γ is defined as follows and compared with observations in Figure 4h:

$$\gamma = \frac{[SO_4^{2-}] + [NO_3^-] + [NH_4^+]}{[SO_4^{2-}] + [NO_3^-] + [NH_4^+] + [EC] + [POC]} \quad (1)$$

In this equation, brackets indicate mass concentrations. Although one should include SOA to calculate secondary aerosol fraction accurately, we did not include it because SOA concentrations were severely underestimated by WRF-CMAQ. Because positive correlation between SO_4^{2-} concentrations and the m/z 44 signal (a good indicator of oxygenated organic aerosols [*Zhang et al.*, 2005]) was obtained by the AMS instrument, the index γ defined by equation (1) is appropriate to represent temporal variations of the secondary aerosol fraction. As seen in Figure 4h, the observed index γ was typically about 0.6 in the stagnant regime, while it decreased to as low as 0.2 upon passage of a cold front or frontal zone. Model calculations successfully reproduced these temporal variations. When clean air with low primary and secondary concentrations is brought into Beijing upon passage of a cold front, intensive and continuous emissions of primary aerosols in and around Beijing result in a very small secondary aerosol fraction γ (see section 6).

[29] In summary, model calculations in this study generally reproduced meteorological and chemical parameters well, except for SO_2, NO_3^-, and SOC (or SOA). The overestimations of SO_2 and NO_3^- were likely due to an overestimation of emissions and precursor species, while the underestimation of SOA was likely due to missing processes or sources in the current organic aerosol model calculations. The agreement found for the other species here indicates that factors and processes affecting aerosol and O_3 concentrations were generally reproduced well in our model calculations, namely emissions of precursors, transport, and photochemical production.

5. Comparison With MODIS AOD Measurements

[30] Spatial distributions of model calculated (WRF-CMAQ) AOD of fine particles were compared with MODIS satellite measurements (level 2 Terra and Aqua fine particle AOD data) [*Remer et al.*, 2005]. Column AOD was estimated from model calculated aerosols using the reconstructed mass extinction (RM) method empirically developed by *Malm et al.* [1994]. This method assumes external mixing of aerosols and was used in CMAQ visibility calculations [*Binkowski and Roselle*, 2003] and previous studies [*Malm et al.*, 2005; *Roy et al.*, 2007]. With this method, AOD is estimated by the following equations:

$$AOD_{calc} = \sum_{i=1}^{N} (b_s + b_a)_i dZ_i \quad (2)$$

$$\begin{aligned} b_s &= 0.003 f(RH)[sulfate + ammonium + nitrate] \\ &\quad + 0.004[OC] + 0.001[others] \\ b_a &= 0.01[EC] \end{aligned} \quad (3)$$

In these two equations, N is the number of vertical layers, dZ_i (m) is the thickness of layer i, and b_s and b_a (m^{-1}) are the light extinction due to aerosol scattering and absorption, respectively. The [x] in equation (3) indicates mass concentration of species x in fine particles (mg m^{-3}). The $f(RH)$ is the aerosol growth factor, which is the ratio of extinction at ambient relative humidity RH and under dry conditions. The $f(RH)$ values provided in a look-up table for ammonium sulfate by *Malm et al.* [1994] were used for all inorganic species as was done in previous studies [*Binkowski and Roselle*, 2003; *Roy et al.*, 2007]. This method is rather

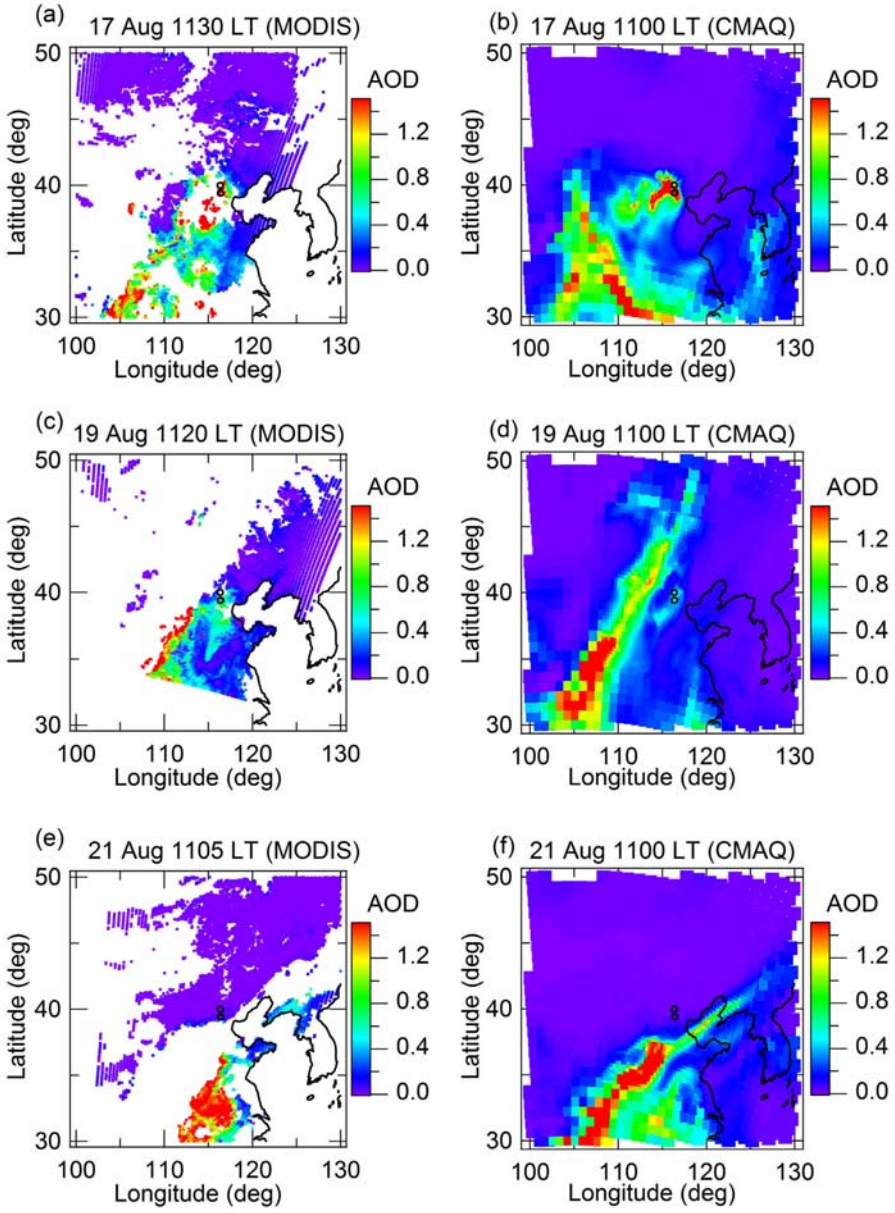

Figure 6. Spatial distribution of aerosol optical depth (AOD) around Beijing obtained from the MODIS satellite and model calculations. Nonshaded areas for MODIS data are cloudy regions or where no data are available.

simple; however, it is considered to be enough to evaluate model performance in calculating the spatial distribution of aerosols through comparison with satellite observations.

[31] Terra and Aqua MODIS measurements were made once per day at local times of about 1100 and 1400, respectively. Three examples of comparisons between MODIS measurements and model calculations are shown in Figures 6a–6f. The MODIS data are shown about 48 h apart, namely on 17, 19, and 21 August. As seen in Figures 6a–6f, regions with high AOD values moved day-to-day in association with synoptic-scale meteorological conditions, and these features were generally reproduced well by the model calculations.

[32] The agreement in AOD values between the MODIS observations and model calculations was evaluated further in a more systematic way as follows. The evaluation was made on each day within the area of 30°–50°N and 100°–130°E by comparing the AOD value in 1 × 1 degree cells (in total 20 × 30 = 600 cells). Because the pixel size of MODIS data used in this study was 10 × 10 km^2, the maximum number of pixels within a 1 × 1 degree cell is approximately 100. These pixel data were averaged to obtain 1 × 1 degree cell data. We discarded cell data when fewer than 25 pixels were available from MODIS measurements due to a limited field of view or the presence of clouds. Averages within 1 × 1 degree cells were used in this study in order to reduce the influence of pixel noise in the MODIS measurements. Furthermore, considering influences of synoptic-scale meteorology, we intended to evaluate the spatial distribution of aerosols on a horizontal scale of about 100 km. The average AOD and R values were calculated for each day

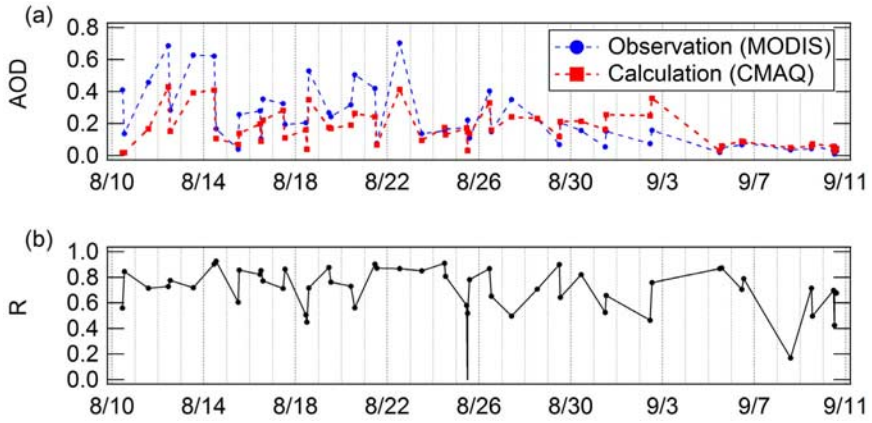

Figure 7. Comparison between the MODIS-derived AOD and model-calculated AOD within the area of 30°–50°N and 100°–130°E. (a) The average of the available data is shown for the MODIS observations, while values for the corresponding cells are averaged for the model calculations so that they can be compared directly. (b) Correlation coefficient between the MODIS observations and model calculations. See text (section 5) for detailed explanations.

using these cell data, when more than 50 cell data were available out of 600 cells. R is an indicator of the agreement of the regional distributions of AOD for each day. Temporal variations of average AOD and R are shown in Figure 7. Although the absolute value of AOD was underestimated, the characteristics of observed temporal variations in average AOD were reproduced well by the model calculations. R values were generally greater than 0.7 when the average AOD was greater than 0.2, indicating that the model calculations captured the spatial inhomogeneity in aerosol concentrations around Beijing.

6. Spatial and Temporal Variations of Aerosols Around Beijing

[33] Because the temporal and spatial distributions of aerosols were generally reproduced well by the model calculations (sections 4 and 5), temporal variations of aerosols around the Beijing area were interpreted using model calculations from the viewpoint of regional-scale aerosol distributions. In Figures 8a, 8c, 8e, and 8g, model calculated $PM_{2.5}$ dry aerosol concentrations at the surface are shown. They are results at 1400 LT (Beijing time) on 16, 18, 20, and 21 August. The time period covered by these four plots corresponds to the beginning of stagnant conditions through the middle of sweeping conditions (Figure 4i). Equivalent potential temperature (θ_e) and horizontal wind vectors (u and v) at 850 hPa derived from NCEP FNL data are also shown for the corresponding dates (Figures 8b, 8d, 8f, and 8h). Wind vectors are Eulerian meteorological parameters showing the wind field at each time, while equivalent potential temperature is a Lagrangian parameter reflecting the nature of air at its origin.

[34] On 16 August, a stationary front was located across the Yellow Sea, and the Beijing area was under the influence of an anticyclonic system (Figure 8b). Because of the stagnant air conditions and high emission rates of aerosols and precursor gases over the Great North China Plain (approximately in the region of 32°–40°N and 112°–120°E, see Figures 2a–2d), aerosol concentrations started to increase over this region. On 18 August, weak southerly winds were dominant around Beijing in association with the anticyclonic circulation, and the 330-K θ_e isopleth (purple line in Figure 8d) had moved north of Beijing. As a result, air with high aerosol concentrations had been transported to Beijing and farther to the north, including regions where anthropogenic emissions are quite low (Figure 8c). On 20 August, a cold front or frontal zone as recognized by a large gradient in θ_e passed over Beijing. Strong northerly winds dominated in the Beijing area, resulting in a southward shift of the location of the 330-K isopleth (Figure 8f). Air with high aerosol concentrations was confined within a narrow band along the frontal zone (warm side), which was forced back to the south in association with eastward movement of the frontal zone (Figure 8e). Northerly wind brought clean air into the cold side of the frontal zone, causing a sharp contrast in aerosol concentrations across the frontal zone. Maximum aerosol concentrations were observed at both the PKU and Yufa sites within the high aerosol concentration band along the frontal zone, and an abrupt decrease was observed upon passage of the frontal zone (Figures 4f and 4g). On 21 August, the high aerosol concentration area had moved farther south (Figure 8g), in association with the movement of the frontal zone (Figure 8h). Aerosol concentrations were still low in Beijing. On 23 August, aerosol concentrations started to increase again under stagnant conditions, similar to that described above for 16 August. During the 1-month observation period, similar cycles repeated on a time scale of about a week. Specifically, similar regional aerosol behaviors were found before and after the passages of cold fronts or frontal zones on 13 and 20 August and 3 and 8 September.

[35] In Figures 9a–9d, average concentrations of EC and SO_4^{2-} aerosols are shown for 48–0 h before and 0–48 h after the passage of frontal zones in Beijing by averaging the four events mentioned above. EC and SO_4^{2-} are chosen to show differences in behaviors of primary and secondary aerosols, respectively, under the given meteorological cycle. Average meteorological fields (θ_e and wind field) for the corresponding time periods are also shown in Figures 9e and 9f. These aerosol distributions and meteorological fields shown here reveal common features among the four events.

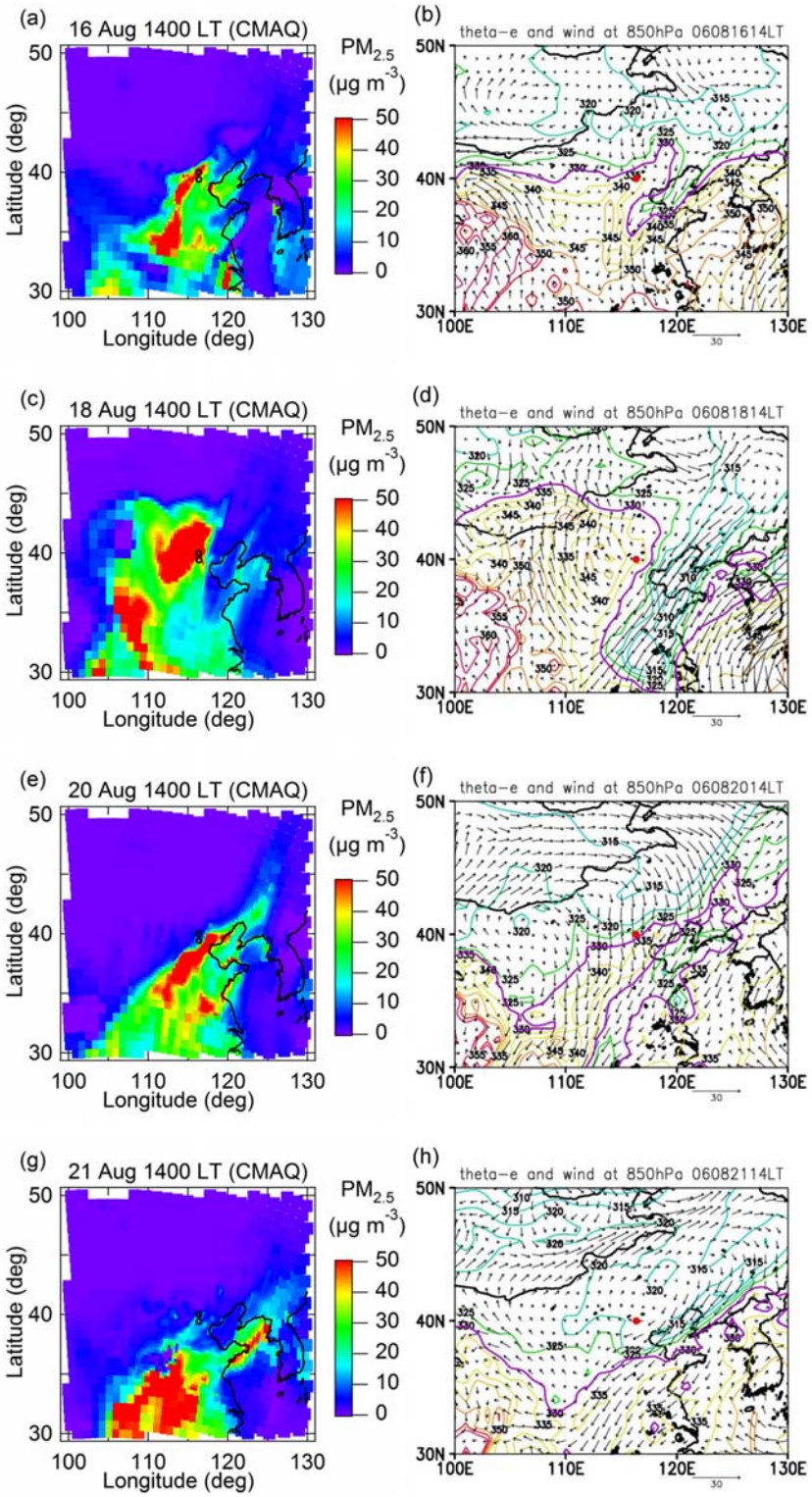

Figure 8. (a, c, e, and g) Spatial distribution of model calculated $PM_{2.5}$ dry aerosol concentrations at the surface (lowest model layer). (b, d, f, and h) Equivalent potential temperature (θ_e, color contour) and horizontal wind vectors (arrows) at the 850-hPa level derived from NCEP FNL data. Isopleths of 330 K θ_e are shown with purple lines. Locations of the PKU and Yufa sites are shown with circles.

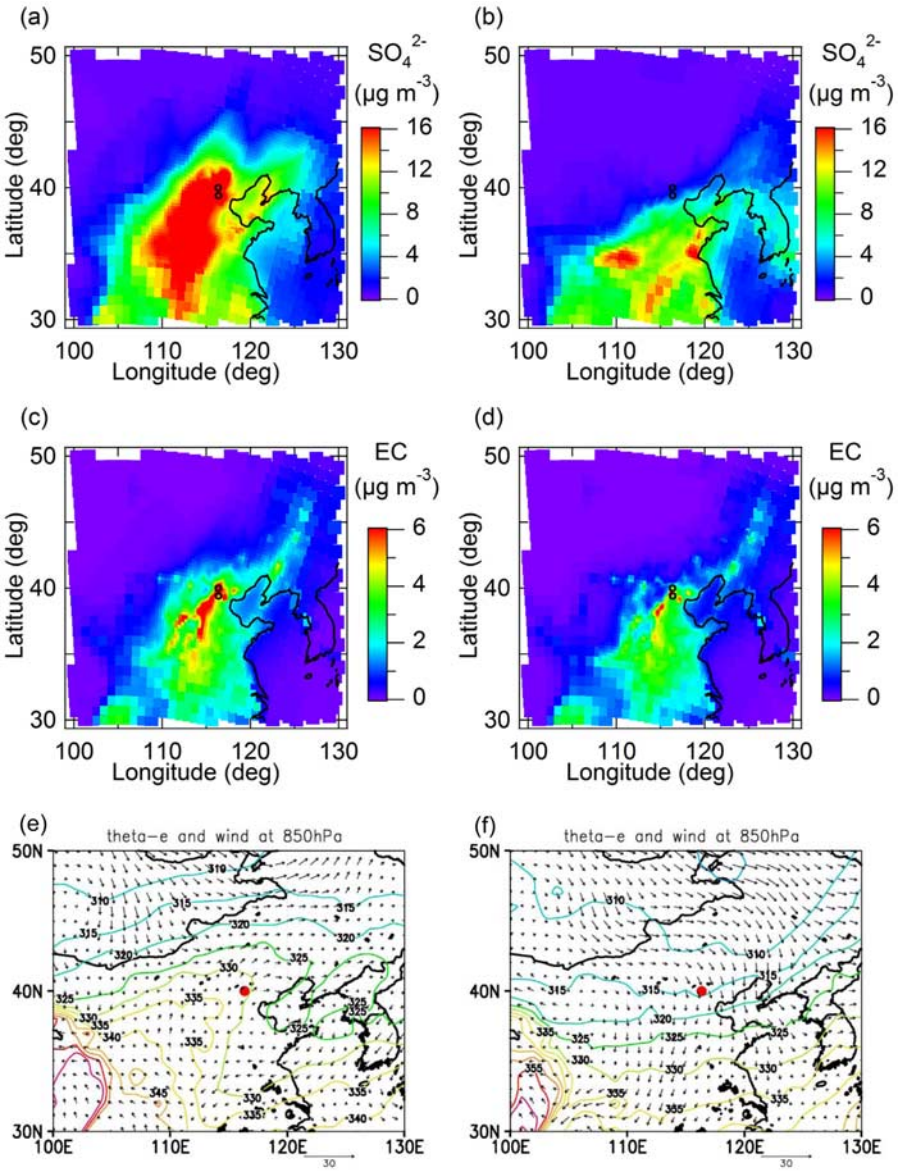

Figure 9. Spatial distributions of model calculated SO_4^{2-} and EC concentration at the surface (lowest model layer) obtained by averaging data from the four cold front (or frontal zone) passage events: 13 and 20 August and 3 and 8 September. (a and c) Concentrations for 48–0 h before the event. (b and d) Concentrations for 0–48 h after the event. (e and f) Equivalent potential temperature (color contour) and horizontal wind vectors (arrows) at the 850-hPa level derived from NCEP FNL data. Locations of the PKU and Yufa sites are shown with circles.

[36] Weak anticyclonic circulation from the middle to the end of the stagnant regime (48–0 h before frontal zone passage, shown in Figure 9e) was favorable to enhance *secondary* aerosol concentrations in and around Beijing in the following two ways. First, stagnant air conditions resulted in enhancements of secondary aerosol concentrations over a large area of about 1000 × 1000 km^2 through the accumulation of aerosols that had been photochemically produced from precursor gases emitted over the Great North China Plain. Second, the southerly wind brought air with high secondary aerosol concentrations to the north of Beijing, resulting in enhancements in and around Beijing. After the passage of the frontal system, strong northerly wind brought clean air from the north and blew high secondary aerosol air away from Beijing. Because of the high secondary aerosol fraction within $PM_{2.5}$ (Figure 4h), these features are similar to those of the $PM_{2.5}$ concentrations shown in Figure 8.

[37] Primary aerosols (EC) behaved differently. They did accumulate in air under stagnant air conditions to some extent by receiving emissions. However, because of a lack of secondary production, concentrations tended to decrease once air left the source region through dilution with cleaner air. Because EC emissions were higher in Beijing as compared with those in surrounding regions, EC concentrations were generally higher in Beijing. As a result, spatial distributions of EC were similar before and after frontal zone passage,

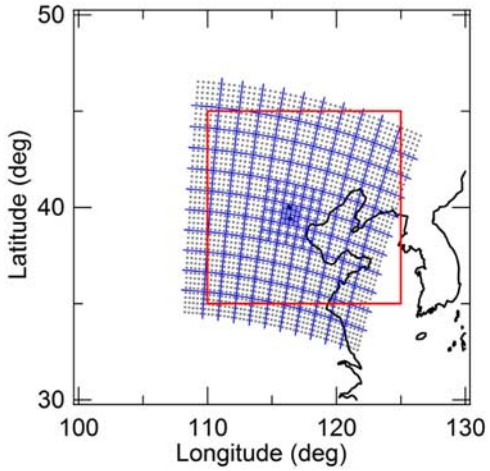

Figure 10. Model cells (blue squares) employed for sensitivity simulations to evaluate contributions of emissions from individual locations. Gray dots denote the grid points (27×27 km^2) of the simulation domain (domain 2). Black circles denote the locations of the PKU and Yufa sites. The red square is the region shown in Figure 11.

although the absolute concentrations were slightly greater during stagnant conditions (Figures 9c and 9d). In particular, high EC concentrations in Beijing reappeared just after frontal zone passage (Figure 9d), and this is in clear contrast to very low SO_4^{2-} concentrations in the same time period (Figure 9b). These mechanisms explain why day-to-day variations were marked for secondary aerosols (Figure 4f), while diurnal variation was more evident for primary aerosols (Figure 4e) in Beijing. These mechanisms are also consistent with the low secondary aerosol fraction during the sweeping regime (Figure 4h).

[38] The results presented in this study clearly show differences in the spatial and temporal variations between primary and secondary aerosols around Beijing under synoptic-scale meteorological conditions. These variations are linked to the locations of emissions, which influenced aerosol concentrations in Beijing and characteristic time scales of aerosol accumulation as presented in section 7.

7. Sensitivity Simulations for Source Apportionment

[39] Two sensitivity studies were made to estimate contributions of emissions in individual areas and time periods to aerosol levels in Beijing. This is a kind of source apportionment study, which provides useful insights for the evaluation of actions to reduce aerosol levels in Beijing. Both primary (EC) and secondary (SO_4^{2-}) aerosols are examined here. First, emissions at each location were increased sequentially to evaluate the resultant changes to aerosol concentrations in Beijing (section 7.1). Second, emissions over the entire model domain were increased during each time period, and the impacts on aerosol concentrations in Beijing were calculated to evaluate how quickly emissions influenced aerosol levels (section 7.2). These two factors are linked together under a given wind field. The linearity of these sensitivity simulations is discussed in Appendix A3.

7.1. Contribution From Emissions at Individual Locations

[40] To evaluate contributions from emissions at individual locations to aerosol levels (EC and SO_4^{2-}) in Beijing, emissions (EC and SO_2) in each grid were individually increased by 20% for the entire time period of the CAREBeijing-2006 campaign. Changes in aerosol concentrations in Beijing resulting from changes in emissions at a particular grid i are expressed by the source contribution (SC_i), which is defined as follows:

$$SC_i = \frac{\sum_t \Delta C_i(t)}{\sum_j \sum_t \Delta C_j(t)} \quad (4)$$

In this equation, $\Delta C_i(t)$ is an incremental change in aerosol concentration (EC or SO_4^{2-}) in Beijing (the PKU site) at time t relative to the base case due to a change in emissions (EC or SO_2) at the ith grid of 20%. Note that the sum of SC_i is unity. Consequently, SC_i is considered to represent the fractional contributions of emissions from individual grids to aerosol concentrations at the PKU site.

[41] In practice, when contributions from emissions at individual locations were estimated, some of the grids were combined together to reduce the number of sensitivity calculations. We call combined grids cells in this section. The cells employed in this study are shown in Figure 10. The cell size was chosen to be smaller at locations near Beijing (27×27 km^2) to resolve local contributions, while the cell size was chosen to be larger at locations farther from Beijing (54×54 or 108×108 km^2). Differences in the areas of individual cells were taken into account when SC_i values were calculated.

[42] Calculations were made for two time periods, namely the "stagnant" and "sweeping" regimes (Figure 4i). In Figures 11a–11d, the spatial distributions of SC_i values are shown for EC and SO_4^{2-} for the two meteorological regimes. In Figure 11, the sum of SC_i values of shaded cells is 0.7, indicating that emissions from these areas accounted for 70% of aerosol concentrations at the PKU site. These cells were selected starting with the cell with the highest SC_i value and adding those with progressively lower SC_i values, until the sum of the SC_i values became 0.7. As seen in Figure 11, there are marked differences in the spatial distributions of SC_i values between primary (EC) and secondary aerosol (SO_4^{2-}) in the stagnant regime (Figures 11a and 11c). In this regime, EC emissions within 100×100 km^2 mostly controlled EC concentrations in Beijing, while SO_2 emissions over 400×500 km^2, including those from the Tianjin Municipality and Hebei Province, affected SO_4^{2-} concentrations. When emissions within a circle with a diameter of 150 km around Beijing was considered, they contributed 73 and 20% of EC and SO_4^{2-} concentrations in Beijing, respectively (Table 5). When SC_i values were calculated for $SO_x = SO_2 + SO_4^{2-}$, their spatial distributions were found to be similar to those of EC (Table 5). Therefore the differences in SC_i values between EC and SO_4^{2-} aerosols were not due to differences in the spatial distributions of emissions, but they reflected differences in their formation processes. EC emissions in Beijing dominated the EC levels in Beijing because of a lack of secondary production and significant

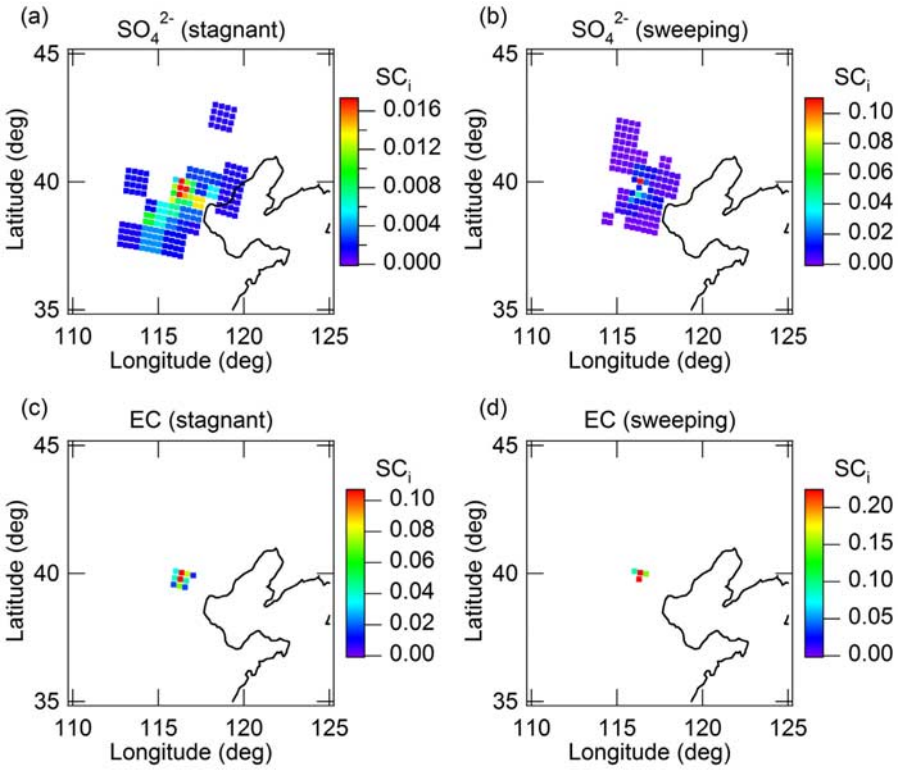

Figure 11. Spatial distribution of source contributions (SC_i) defined by equation (4) for the two atmospheric regimes: (a and c) Stagnant regime; (b and d) sweeping regime. SC_i shows contributions of emissions from individual cells to the concentration of each species at the PKU site (see text in section 7.1 for detailed explanations). Shaded regions are those where the sums of the highest SC_i values is equal to 0.7. The maxima of the color bars (red) are SC_i at the PKU site, which are species- and period-dependent.

emissions in this region as compared to those of surrounding regions. On the other hand, it takes some time to produce inorganic aerosols in the atmosphere from their precursor gases. Even though SO_2 emissions are significant in Beijing, the contribution to SO_4^{2-} levels in Beijing is much less significant. Under stagnant meteorological conditions, slowly moving air parcels received considerable amounts of emissions, such as SO_2, over the source region, and continuous secondary production resulted in accumulation of inorganic aerosols, as discussed in section 6. SO_2 emissions east or north of Beijing had some contribution because of the clockwise air circulation under the influence of anticyclones (see Figure 9e).

[43] In contrast, during the sweeping regime, the spatial extent of shaded cells for SO_4^{2-} (the area in which the sum of SC_i values becomes 0.7) was systematically smaller as compared with that for stagnant air conditions (Figure 11b). The contributions of emissions within a 150-km circle around Beijing were 34 and 20% for the sweeping and stagnant regimes, respectively. Owing to a lack of significant SO_2 emission sources to the north of Beijing and rapid dilution caused by strong winds, the relative contribution of emissions within Beijing became more important in the sweeping regime. The contrast between the stagnant and sweeping regimes was less pronounced for EC (Figures 11c and 11d). These results indicated that the significant emissions within Beijing dominated EC levels in Beijing for all meteorological conditions during the campaign (Table 5).

[44] In summary, primary aerosols such as EC in Beijing were mostly controlled by local emissions within 100–150 km, while secondary aerosols such as SO_4^{2-} were influenced by emissions from the Tianjin Municipality and Hebei Province within a distance as far as 500 km under stagnant conditions. Consequently, because of significant contributions

Table 5. Summary of the Sensitivity Simulations for Source Apportionment

Item	Period	CO	SO_2	EC	Sulfate	SO_x[a]
Contribution within d = 150-km circle (%)	Stagnant	79	82	73	20	75
	Sweeping	90	95	92	34	93
Distance (d) to Σ SC = 0.7 (km)	Stagnant	108	108	120	549	109
	Sweeping	55	55	55	394	55
Age of air (day)	Stagnant	0.37	0.31	0.45	1.38	0.46
	Sweeping	0.16	0.13	0.21	0.52	0.17

[a]SO_x is sum of SO_2 and aerosol sulfate (SO_4^{2-}).

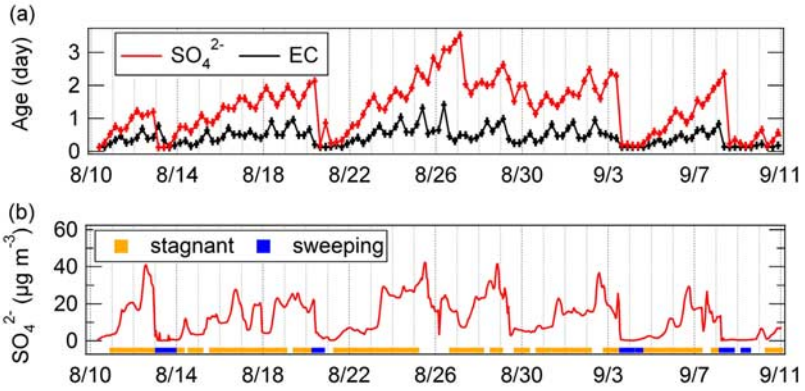

Figure 12. (a) Age of air (τ) defined by equation (5) for EC (black) and sulfate (red) at the PKU site. Vertical (±0.125 day) and horizontal lines (±3 h) denote the resolution of the sensitivity simulations. (b) Model-calculated sulfate concentrations at the PKU site. The meteorological regime is also shown.

of secondary aerosols in Beijing, emission controls should be made over a regional scale (~500 km) in order to improve air quality in Beijing.

7.2. Age of Air in Terms of Aerosol Concentration

[45] We also conducted another set of sensitivity simulations in which emissions (EC or SO_2) over the entire domain 2 were increased during sequential 6-h periods, and the resultant changes in aerosol concentrations (EC and SO_4^{2-}) in Beijing were calculated to evaluate how quickly emissions influenced aerosol levels. As a measure of the time scale of influence, an age of air $\tau(t)$ (day) was defined as a function of date t as follows:

$$\tau(t) = \frac{\sum_k \{(k - 0.5) \times \Delta C_k(t)\}}{\sum_k \Delta C_k(t)} \quad (5)$$

In this equation, $\Delta C_k(t)$ is an incremental change in aerosol concentration (EC or SO_4^{2-}) in Beijing (the PKU site) at time t relative to the base case due to a change in emissions (EC or SO_2) of 20% (over the entire model domain) for the time period between dates $t - k$ and $t - k + 1$. For example, the $\Delta C_k(t)$ value with $k = 1$ is obtained by changing emissions during the preceding 24 h ($t - 1$ to t). If only emissions in this time period affect aerosol levels, the age of air $\tau(t)$ becomes 0.5. In practice, $\tau(t)$ values were calculated every 6 h to resolve diurnal changes in the age of air.

[46] A time series of $\tau(t)$ values of EC and SO_4^{2-} in Beijing are shown in Figure 12. It can be clearly seen in Figure 12 that $\tau(t)$ values were systematically greater for SO_4^{2-} than EC. The averages over a month (all weather conditions) were 0.44 and 1.3 days for EC and SO_4^{2-}, respectively. These results indicate that EC concentrations in Beijing were generally controlled by EC emissions within the preceding 24 h, while SO_2 emissions within the preceding 3 days (1.3 × 2 = 2.6 days) could affect SO_4^{2-} concentrations in Beijing. Because the secondary formation of aerosols takes time, it is reasonable that $\tau(t)$ values were greater for secondary aerosols (SO_4^{2-}) than primary aerosols (EC). In fact, the lifetime of SO_2 against gas phase reaction with OH was estimated to be 5 days when diurnally averaged model calculated OH concentration in Beijing was used. $\tau(t)$ values of EC estimated here are consistent with the fact that EC concentrations in Beijing were generally controlled by local emissions within 100 km, as shown in section 7.1, considering typical wind speeds of 1–2 m s^{-1} or 90–170 km d^{-1}. The results for SO_4^{2-} are also consistent with the fact that SO_4^{2-} concentrations in Beijing were affected by SO_2 emissions as far as 500 km away.

[47] Figure 12 also shows that $\tau(t)$ values of SO_4^{2-} had large day-to-day variations, positively correlated with SO_4^{2-} concentration. Both SO_4^{2-} concentration and $\tau(t)$ values were greater in the stagnant air regime ($\tau(t)$ = 2 to 3 days), and both of them suddenly decreased upon passage of a cold front or frontal zone ($\tau(t)$ = 0.5 days, Table 5). These results reveal the typical time scale of SO_4^{2-} accumulation, especially for the stagnant regime, that is responsible for high aerosol episodes in and around Beijing. An increase in SO_4^{2-} due to a high production rate overcomes the decrease due to dilution up to 3 days after the emission so that SO_2 emissions during the preceding 3 days affect SO_4^{2-} concentrations in Beijing. Because of slow dilution under stable air conditions, accumulation lasts longer, and longer $\tau(t)$ values result. The contrast in $\tau(t)$ values between the two meteorological regimes was much less pronounced for EC. This result is in accordance with the fact that EC emissions within Beijing dominated EC levels in Beijing for all meteorological conditions during the campaign (Table 5).

[48] The sensitivity simulations presented in sections 7.1 and 7.2 focused on influences on aerosol levels in Beijing (Beijing was chosen as a receptor), because intensive measurements had been made during the campaign and air quality in this region is important for the large number of people living there. We conducted a series of similar sensitivity simulations by setting other locations within domain 2 as receptors. As a result, essentially the same relative relationship was found among SC_i values or ages of air between primary and secondary aerosols (higher SC_i values and ages for secondary aerosols than primary aerosols), although the absolute values were different depending on the location. These results indicate that the conclusions presented in this section can be considered general at least in the northeast part of China.

[49] It is finally noted that the age of air defined by equation (5) is a new concept in this study. The age is

estimated for individual species depending on the characteristic times of accumulation, formation, dilution, and deposition. It therefore has several advantages in understanding the behavior of atmospheric species, as demonstrated in this study.

8. WRF-chem Calculations and Comparison With WRF-CMAQ

8.1. WRF-chem Model

[50] In this study, results of WRF-chem model calculations were compared with WRF-CMAQ calculations and observations in order to quantify uncertainties in the model predictions. WRF-chem (version 2.2) is an online model, which simulates trace gases and aerosols simultaneously with the meteorological fields using a common transport scheme and vertical mixing parameterizations [*Grell et al.*, 2005; *Fast et al.*, 2006]. For meteorological calculations, the same parameterization schemes and options that had been employed for WRF-CMAQ calculations were used (Table 2). As for WRF-CMAQ calculations, analysis nudging was applied in WRF-chem calculations using NCEP FNL data. As a result, meteorological fields were similar between the two models (Figures 4a and 4b). Some differences in wind direction were occasionally seen under calm wind conditions (<1 m s^{-1}).

[51] In contrast to the meteorological calculations, several different options were adopted for WRF-chem chemistry calculations (Table 2). For the gas phase chemistry, we used CBM-Z, an updated lumped structure gas phase photochemical mechanism that is based on the CBM-IV mechanism [*Zaveri and Peters*, 1999]. Photolysis rates were calculated by the Fast-J scheme [*Wild et al.*, 2000; *Barnard et al.*, 2004]. For the aerosol module, MOSAIC was used in which a sectional representation for the aerosol size distribution was adopted to simulate both the number and mass in each aerosol size bin [*Fast et al.*, 2006; *Zaveri et al.*, 2005a, 2005b, 2008]. An 8-size-bin representation was adopted in this study. Aerosol species include SO_4^{2-}, NO_3^-, NH_4^+, EC, POC, other inorganics (nonreactive dust), and aerosol water. Aqueous chemistry [*Fahey and Pandis*, 2001] and in-cloud and below-cloud wet removal of aerosol particles [*Easter et al.*, 2004] are also represented in the WRF-chem model.

[52] For WRF-chem calculations, only domains 2 and 3 (smaller two regions in Figure 1) were employed in order to reduce the computational time, and the chemical boundary conditions of domain 2 were derived from the results of CMAQ calculations for domain 1. Two-way nesting was conducted for WRF-chem calculations. The emission inventories adopted in WRF-chem calculations were the same as those used in WRF-CMAQ calculations, although the speciation of some VOCs is different between the SAPRC and CBM-Z gas phase mechanisms.

8.2. Comparison With Observations and WRF-CMAQ Calculations

[53] The results of the WRF-chem calculations are shown in Figures 4a–4h (orange lines) and Table 6. As shown, WRF-chem calculations reproduced the observed features of temporal variations of meteorological and chemical parameters reasonably well at both the PKU and Yufa sites. The levels of agreements were similar between the WRF-chem and WRF-CMAQ calculations, as indicated by, for example, similar R values between the models (Table 4 for WRF-CMAQ; Table 6 for WRF-chem).

[54] When we compared the results of the WRF-chem model with those of the WRF-CMAQ model at the PKU and Yufa sites, it was found that concentrations of primary species, such as CO, NO_x, SO_2, POC, and EC, were generally greater in the WRF-chem model (Tables 4 and 6). For example, EC concentrations calculated using the WRF-chem model were greater by 20% at both sites. The most probable reason for these differences is the difference in the vertical mixing treatment between the models, because column EC concentrations agreed within 10%. This fact is confirmed by the systematic difference in vertical profiles of EC shown in Figure 5. Even though both models utilize the WRF model with the same options to calculate meteorological parameters (Table 2), the way the vertical eddy diffusion coefficient (K_z) is calculated is different between the models. In the WRF-chem model, the vertical mixing process of chemical species was calculated in a way consistent with the vertical mixing of heat and moisture [*Grell et al.*, 2005; *Hong et al.*, 2006]. This approach is good in principle; however, it was reported that the simple use of the same parameterization and K_z values for chemical species with those of meteorological parameters could result in too little vertical mixing during the night, leading to unreasonably high concentrations of primary pollutants at the surface [*McKeen et al.*, 2007]. On the other hand, because CMAQ is an offline model, K_z and the vertical mixing process of chemical species are calculated with a method that is not necessarily consistent with the meteorological calculations [*Byun and Ching*, 1999]. *Byun et al.* [2007] reported that the CMAQ model tends to give higher K_z values resulting in more efficient vertical mixing within the planetary boundary layer in daytime as compared with the CAMx model. When K_z values were examined in this study, they frequently reached predetermined minimum values of 1.0 and 0.1 m^2 s^{-1} in the WRF-CMAQ and WRF-chem models, respectively, during the night. Because of these systematically lower K_z values calculated by WRF-chem, higher concentrations of primary species at the surface were predicted (Figure 5). Using the CMAQ model, *Zhang et al.* [2006] also reported that PM concentrations during the night largely depended on the choice of the minimum K_z values between 1.0 and 0.1 m^2 s^{-1}. During the daytime, WRF-chem K_z values were also generally lower at altitudes above 500 m, which is also consistent with vertical profiles of EC shown in Figure 5. These results show levels of uncertainties in model predictions of primary species resulting from boundary layer processes. Systematic understanding of the causes of these differences is beyond the scope of this paper. It is noted, however, that in spite of the differences in the absolute concentrations, temporal variations in the primary species were quite similar between the two models, primarily owing to the similar meteorological field calculated using the WRF models.

[55] Concentrations of inorganic species (SO_4^{2-}, NO_3^-, and NH_4^+) predicted by the two model calculations agreed to within 20 and 10% at the PKU and Yufa sites, respectively. Better agreements in secondary aerosol predictions than those for primary aerosols were obtained because concentrations of secondary aerosols at the surface were generally less affected by differences in vertical mixing processes. This was due to

Table 6. Evaluation Statistics for Meteorological and Chemical Components Calculated by WRF-chem

Component	Units	Average		RMSE[a]	MB[a]	NMB[a] (%)	R[a]	
		Measured	Calculated				Hourly	Daily[b]
PKU Site								
Temperature	K	299.0	299.6	2.48	0.59	0.20	0.87	0.88
Relative humidity	%	63.9	53.3	15.3	−10.6	−16.5	0.84	0.88
Wind speed	m s^{-1}	1.44	2.55	1.60	1.10	76.4	0.61	0.81
Wind speed (U)	m s^{-1}	0.47	0.46	–	–	–	0.37	0.77
Wind speed (V)	m s^{-1}	−0.026	0.46	–	–	–	0.54	0.70
CO	ppbv	1159	1107	681	−51.6	−4.45	0.43	0.49
O_3	ppbv	28.8	33.2	20.5	4.38	15.2	0.82	0.67
NO_x	ppbv	38.5	60.9	50.2	22.5	58.3	0.53	0.44
SO_2	ppbv	8.62	53.8	61.6	45.2	524	0.057	0.45
Ethane	ppbv	2.95	2.01	1.41	−0.94	−32.0	0.60	0.64
Alkanes (C_3–C_8)	ppbv	17.0	11.3	16.0	−5.71	−33.6	0.22	0.36
Alkenes (C_2–C_5)	ppbv	6.55	5.42	4.58	−1.13	−17.2	0.034	−0.13
Toluene	ppbv	3.93	1.14	3.93	−2.78	−70.9	0.40	0.46
Xylene	ppbv	1.74	0.58	1.55	−1.16	−66.9	0.40	0.35
Sulfate	μg m^{-3}	33.2	12.7	31.9	−20.5	−61.8	0.65	0.72
Ammonium	μg m^{-3}	20.5	12.0	16.5	−8.52	−41.5	0.44	0.77
Nitrate	μg m^{-3}	24.2	20.5	21.2	−3.65	−15.1	0.42	0.78
EC	μg m^{-3}	6.21	11.4	7.61	5.22	84.1	0.69	0.66
POC	μg m^{-3}	6.77	12.4	7.66	5.64	83.4	0.71	0.70
Yufa Site								
Temperature	K	297.3	299.0	2.74	1.74	0.58	0.89	0.90
Relative humidity	%	68.7	56.4	18.0	−12.3	−17.9	0.72	0.79
Wind speed	m s^{-1}	1.77	3.07	1.95	1.30	73.3	0.57	0.80
Wind speed (U)	m s^{-1}	0.15	0.15	–	–	–	0.37	0.70
Wind speed (V)	m s^{-1}	0.59	0.47	–	–	–	0.57	0.85
CO	ppbv	771	1132	654	361	46.8	0.36	0.58
O_3	ppbv	36.1	27.8	21.9	−8.38	−23.2	0.76	0.32
NO_x	ppbv	15.0	62.5	65.2	47.6	317	0.43	0.24
SO_2	ppbv	7.16	48.7	52.5	41.5	580	−0.15	0.35
Ethane	ppbv	4.65	2.55	5.42	−2.11	−45.3	0.40	0.48
Alkanes (C_3–C_8)	ppbv	10.5	13.6	16.3	3.14	29.9	0.30	0.39
Alkenes (C_2–C_5)	ppbv	3.65	5.21	5.39	1.56	42.8	0.19	0.018
Toluene	ppbv	3.38	1.09	10.1	−2.29	−67.6	−0.068	−0.087
Xylene	ppbv	2.26	0.72	12.1	−1.54	−68.2	−0.083	0.037
Sulfate	μg m^{-3}	10.8	12.0	9.53	1.23	11.4	0.50	0.54
Ammonium	μg m^{-3}	4.74	10.2	8.60	5.47	115	0.58	0.60
Nitrate	μg m^{-3}	3.97	19.8	23.1	15.8	398	0.68	0.61
EC	μg m^{-3}	4.89	11.1	7.89	6.18	126	0.51	0.57
POC	μg m^{-3}	3.91	12.1	9.45	8.22	210	0.61	0.59
$PM_{2.5}$	μg m^{-3}	80.9	90.0	47.1	9.02	11.1	0.61	0.74

[a]Definitions are given by equations (A1)–(A4) in Appendix A2.
[b]The correlation coefficient is calculated for daytime averages (0900–1600 LT).

smaller vertical gradients in secondary aerosol mixing ratios resulting from production within the atmosphere. A smaller vertical gradient also explained smaller diurnal variations of secondary aerosols as discussed in section 4.

[56] WRF-chem predicted systematically lower O_3 concentrations as compared with those of WRF-CMAQ calculations at both sites. Since both models predicted similar $O_3 + NO_2$ concentrations, the lower O_3 concentrations in WRF-chem calculations than those in WRF-CMAQ calculations were mainly due to the larger NO_x concentrations at surface, leading to too much titration by NO.

[57] So far, WRF-chem and WRF-CMAQ model calculations have been compared only at the two intensive sites at Yufa and PKU. Agreements in the three-dimensional aerosol distributions over domain 2 between the two models are also evaluated in this study. In order to evaluate similarities in spatial distributions of aerosols, we calculated correlation coefficients (R) using diurnal mean $PM_{2.5}$ concentrations predicted by these two models. The daily R values of surface dry $PM_{2.5}$ mass concentrations and column-integrated dry $PM_{2.5}$ mass concentrations were 0.83 ± 0.13 and 0.81 ± 0.16, respectively, suggesting that the two models predicted similar spatial aerosol distributions during the CAREBeijing-2006 campaign.

9. Summary

[58] Regional aerosol model calculations were made using the WRF-CMAQ model to study spatial and temporal variations of aerosols around Beijing, China, in the summer of 2006, when the CAREBeijing-2006 campaign was conducted. To quantify uncertainties in the model predictions, WRF-chem calculations were also compared with observations and WRF-CMAQ calculations. Both model calculations generally reproduced well the temporal variations of observed meteorological parameters and concentrations of gaseous and aerosol species both at the PKU urban site and Yufa suburban site. Spatial distributions of model calculated AOD using WRF-CMAQ also agreed well with MODIS satellite measurements over northeast China, suggesting the validity of regional aerosol distributions predicted by the model. The agreements with in situ and satellite data

indicate that factors and processes affecting aerosol and O_3 concentrations around Beijing were generally reproduced well in our model calculations, namely emissions, transport, and photochemical production. Although the WRF-chem model showed performance similar to that of WRF-CMAQ, systematically greater concentrations of primary species at the surface were predicted, suggesting some inconsistencies between the models in calculating mixing processes within the planetary boundary layer.

[59] Enhancements in secondary (inorganic) aerosol concentrations were simultaneously observed at the PKU and Yufa sites 4 or 5 times during a 1-month observation period. Model calculations reproduced these features well and showed that weak anticyclonic circulation during the stagnant period resulted in enhancements of secondary aerosol concentrations over a large area on a scale of 1000×1000 km^2. The enhancements resulted from the accumulation of aerosols that had been photochemically produced from precursor gases emitted over the Great North China Plain. The southerly wind of anticyclonic circulation brought air with high secondary aerosol concentrations to Beijing and farther to the north. On the contrary, after the passage of a frontal system, strong northerly winds brought clean air from the north and transported high secondary aerosol air away from Beijing. A series of these variations were repeated on a time scale of about a week. Sensitivity studies showed that under stagnant air conditions SO_2 emissions over 400×500 km^2, including those from the Tianjin Municipality and Hebei Province, affected SO_4^{2-} concentrations in Beijing. SO_2 emissions within a 150-km circle around Beijing contributed only 20% of the SO_4^{2-} concentration. Further analyses showed that emissions within the preceding 3 days could affect secondary aerosol concentrations. In other words, the time scale of SO_4^{2-} accumulation resulting in enhancement in SO_4^{2-} concentrations in Beijing was about 3 days.

[60] In contrast to the slow temporal variation of secondary aerosols (inorganic aerosols), diurnal variation was evident for primary aerosols, such as EC, owing to accumulation of pollutants in association with lower planetary boundary layer height during nighttime. Primary aerosols accumulated in air under stagnant air conditions to some extent; however, because of a lack of secondary production, concentrations tended to decrease once air left Beijing though dilution with cleaner air. As a result, the spatial distributions of EC were similar before and after frontal zone passage. In fact, high EC concentrations in Beijing reappeared immediately after frontal zone passage, in clear contrast to very low SO_4^{2-} concentrations during the same time period. As a result, the secondary aerosol fraction became systematically lower during the sweeping regime as compared with that in the stagnant regime. Sensitivity studies showed that under the stagnant and sweeping air conditions, EC emissions within a 150-km circle around Beijing contributed 73 and 92%, respectively, of the EC levels in Beijing. Emissions within the preceding 24 h affected EC concentrations.

[61] In this study temporal variations of primary and secondary aerosols observed in Beijing were described from the viewpoint of regional aerosol distributions, which are controlled by emission distributions, meteorological fields, and photochemical production processes. Because secondary aerosols comprise a considerable fraction of fine particles, the results presented in this study suggest that emission controls should be made over a regional scale ($\sim$500 km) in order to improve air quality in Beijing. The temporal variations of inorganic aerosols and EC concentrations as well as their ratios control the optical properties of aerosols that affect the radiation budget over the Beijing area. This will be described in a paper in preparation (H. Matsui et al., Spatial and Temporal Variations of Aerosols around Beijing in Summer 2006: 2. Local and Column Aerosol Optical Properties, manuscript in preparation, 2009).

Appendix A

A1. Sensitivity Simulations Using Scaled Emissions

[62] As shown in section 3.2, model calculated NO_x/CO, SO_x/CO, EC/CO, and POC/CO ratios were greater than observations at both the PKU and Yufa sites by factors of 1.9, 4.1, 2.1, and 1.9, respectively. These results indicate that there were some inconsistencies in emission data among the species. Sensitivity studies presented in section 7 show that 70–100% of concentrations of primary species in Beijing were controlled by emissions within a 150-km circle around Beijing (Table 5). Consequently, we conducted sensitivity simulations in which emissions within the 150-km area around Beijing were scaled so that emission ratios agreed with observations. Specifically, we did not change CO emissions but reduced emissions of NO_x, SO_2, EC, POC, and Other PM (nonreactive dust) by factors of 2, 5, 2, 2, and 2, respectively. As a result, model calculated concentrations of NO_x, SO_2, EC, and POC changed by -52, -72, -41, and -37%, respectively, on average. The ratios of model calculation to observed concentration were 0.62, 1.34, 0.86, and 0.85 at the PKU site. On the other hand, SO_4^{2-}, NO_3^-, and NH_4^+ aerosols changed by only -17, -11, and -15%, respectively. These results suggest that even if an overestimation in SO_2 emissions was confined to within a 150-km distance around Beijing, the results presented in this study do not change significantly. If SO_2 emissions over a wider region around Beijing were overestimated, the contribution of SO_2 emissions farther than 500 km could affect the SO_4^{2-} concentrations in Beijing, although emissions within the area within 500 km were estimated to be responsible in this study (section 7).

A2. Definitions for Statistical Evaluation

[63] The definitions of the quantities to evaluate model performance used in sections 4 and 5 are described here. The agreement between measurements and model calculations was evaluated using the following four quantities: root mean square error (RMSE), mean bias (MB), normalized mean bias (NMB), and correlation coefficient (R), which are defined below:

$$RMSE = \sqrt{\frac{1}{N}\sum_{i=1}^{N}\{C_{model}(t_i) - C_{obs}(t_i)\}^2} \quad \text{(A1)}$$

$$MB = \frac{1}{N}\sum_{i=1}^{N}\{C_{model}(t_i) - C_{obs}(t_i)\} \quad \text{(A2)}$$

$$NMB = \frac{\sum_{i=1}^{N} \{C_{model}(t_i) - C_{obs}(t_i)\}}{\sum_{i=1}^{N} C_{obs}(t_i)} \times 100 \quad \text{(A3)}$$

$$R = \frac{\sum_{i=1}^{N} \left\{C_{model}(t_i) - \overline{C_{model}}\right\}\left\{C_{obs}(t_i) - \overline{C_{obs}}\right\}}{\sqrt{\sum_{i=1}^{N} \left\{C_{model}(t_i) - \overline{C_{model}}\right\}^2 \sum_{i=1}^{N} \left\{C_{obs}(t_i) - \overline{C_{obs}}\right\}^2}} \quad \text{(A4)}$$

where C_{obs} and C_{model} refer to observed and model calculated quantities of various parameters, respectively, and N refers to the number of data points. The overbar in equation (A4) denotes averages of N data points.

A3. Linearity in Sensitivity Simulations

[64] In conducting sensitivity studies described in section 7, a linear relationship between emissions and aerosol concentrations was implicitly assumed. The degree of linearity is discussed here by showing two comparisons. First, we checked the linearity between aerosol concentrations in Beijing and emissions over the whole model domain (domain 2 shown in Figure 1). We simply changed emissions (EC and SO_2) over the whole model domain by 20% and examined changes in aerosols (EC and SO_4^{2-}) in Beijing. As a result, the mean concentrations in Beijing changed by 19.8 and 17.6% for EC and SO_4^{2-}, respectively. The increase in SO_4^{2-} was slightly lower than the increase in SO_2 emissions, likely due to SO_4^{2-} flux from outside the model domain and a decrease in OH concentration resulting from the increase in SO_2 emissions.

[65] Second, we checked the linearity between aerosol concentrations at Beijing and emissions from individual locations. We changed emissions (EC and SO_2) at each location one by one by 20% and evaluated aerosol concentrations (EC and SO_4^{2-}) in Beijing for each case. The sums of the aerosol changes were compared with aerosol changes resulting when emissions over the whole model domain were simultaneously increased by 20%. Reasonable agreement was found between the two cases. A similar exercise was done for sensitivity studies in which emissions in each time period were increased by 20%. Reasonable agreement was also found, indicating the validity of the method adopted in this study.

[66] **Acknowledgments.** We are indebted to all of the CAREBeijing-2006 campaign participants for their cooperation and support. Special thanks are due to the staff and students from the Peking University for leading and carrying out this project. We would like to thank W. I. Gustafson, Jr. at PNNL for providing useful comments on WRF-chem model calculations. This study was supported by the Ministry of Education, Culture, Sports, Science, and Technology (MEXT) in Japan. This study was also supported in part by the Alliance for Global Sustainability (AGS) project, University of Tokyo. This study was conducted as a part of the Megacities Asia Task under the framework of the International Global Atmospheric Chemistry (IGAC) project.

References

An, X., T. Zhu, Z. Wang, C. Li, and Y. Wang (2007), A modeling analysis of a heavy air pollution episode occurred in Beijing, *Atmos. Chem. Phys.*, *7*, 3103–3114.

Barnard, J. C., E. G. Chapman, J. D. Fast, J. R. Schmelzer, J. R. Schlusser, and R. E. Shetter (2004), An evaluation of the Fast-J photolysis model for predicting nitrogen dioxide photolysis rates under clear and cloudy sky conditions, *Atmos. Environ.*, *38*, 3393–3403, doi:10.1016/j.atmosenv.2004.03.034.

Binkowski, F. S., and S. J. Roselle (2003), Models-3 Community Multiscale Air Quality (CMAQ) model aerosol component: 1. Model description, *J. Geophys. Res.*, *108*(D6), 4183, doi:10.1029/2001JD001409.

Bond, T. C., D. G. Streets, K. F. Yarber, S. M. Nelson, J.-H. Woo, and Z. Klimont (2004), A technology-based global inventory of black and organic carbon emissions from combustion, *J. Geophys. Res.*, *109*, D14203, doi:10.1029/2003JD003697.

Byun, D. W., and J. K. S. Ching (1999), Science algorithms of the EPA Models-3 Community Multiscale Air Quality (CMAQ) modeling system, *Rep. EPA/600/R-99/030*, U.S. Environ. Prot. Agency, Washington, D. C.

Byun, D. W., S.-T. Kim, and S.-B. Kim (2007), Evaluation of air quality models for the simulation of a high ozone episode in the Houston metropolitan area, *Atmos. Environ.*, *41*, 837–853, doi:10.1016/j.atmosenv.2006.08.038.

Carter, W. P. L. (2000), Documentation of the SAPRC-99 chemical mechanism for VOC reactivity assessment: Final report to California Air Resources Board, *Contracts 92–329 and 95–308*, Statewide Air Pollut. Res. Cent., Univ. of Calif., Riverside.

Chan, C. K., and X. Yao (2008), Air pollution in mega cities in China, *Atmos. Environ.*, *42*, 1–42, doi:10.1016/j.atmosenv.2007.09.003.

Chang, S. Y., C. T. Lee, C. C. K. Chou, S. C. Liu, and T. X. Wen (2007), The performance comparison of the in situ IC instrument and the continuous field measurements of soluble aerosol compositions at the Taipei Aerosol Supersite, Taiwan, *Atmos. Environ.*, *41*, 1936–1949, doi:10.1016/j.atmosenv.2006.10.051.

Chen, D. S., S. Y. Cheng, L. Liu, T. Chen, and X. R. Guo (2007), An integrated MM5-CMAQ modeling approach for assessing trans-boundary PM10 contribution to the host city of 2008 Olympic summer gases: Beijing, China, *Atmos. Environ.*, *41*, 1237–1250, doi:10.1016/j.atmosenv.2006.09.045.

Colman, J. J., A. L. Swanson, S. Meinardi, B. C. Sive, D. R. Blake, and F. S. Rowland (2001), Description of the analysis of a wide range of volatile organic compounds in whole air samples collected during PEM-Tropics A and B, *Anal. Chem.*, *73*, 3723–3731, doi:10.1021/ac010027g.

Easter, R. C., S. J. Ghan, Y. Zhang, R. D. Saylor, E. G. Chapman, N. S. Laulainen, H. Abdul-Razzak, L. R. Leung, X. Bian, and R. A. Zaveri (2004), MIRAGE: Model description and evaluation of aerosols and trace gases, *J. Geophys. Res.*, *109*, D20210, doi:10.1029/2004JD004571.

Fahey, K. M., and S. N. Pandis (2001), Optimizing model performance: Variable size resolution in cloud chemistry modeling, *Atmos. Environ.*, *35*, 4471–4478, doi:10.1016/S1352-2310(01)00224-2.

Fast, J. D., W. I. Gustafson Jr., R. C. Easter, R. A. Zaveri, J. C. Barnard, E. G. Chapman, G. A. Grell, and S. E. Peckham (2006), Evolution of ozone, particulates, and aerosol direct radiative forcing in the vicinity of Houston using a fully coupled meteorology-chemistry-aerosol model, *J. Geophys. Res.*, *111*, D21305, doi:10.1029/2005JD006721.

Garland, R. M., et al. (2009), Aerosol optical properties observed during Campaign of Air Quality Research in Beijing 2006 (CAREBeijing-2006): Characteristic differences between the inflow and outflow of Beijing city air, *J. Geophys. Res.*, *114*, D00G04, doi:10.1029/2008JD010780.

Grell, G. A., S. E. Peckham, R. Schmitz, S. A. McKeen, G. Frost, W. C. Skamarock, and B. Eder (2005), Fully coupled "online" chemistry within the WRF model, *Atmos. Environ.*, *39*, 6957–6975, doi:10.1016/j.atmosenv.2005.04.027.

Griffin, R. J., D. R. Cocker III, R. C. Flagan, and J. H. Seinfeld (1999), Organic aerosol formation from the oxidation of biogenic hydrocarbons, *J. Geophys. Res.*, *104*, 3555–3567, doi:10.1029/1998JD100049.

Guenther, A., et al. (1995), A global model of natural volatile organic compound emissions, *J. Geophys. Res.*, *100*, 8873–8892, doi:10.1029/94JD02950.

Gustafson, W. I., Jr., E. G. Chapman, S. J. Ghan, R. C. Easter, and J. D. Fast (2007), Impact on modeled cloud characteristics due to simplified treatment of uniform cloud condensation nuclei during NEAQS 2004, *Geophys. Res. Lett.*, *34*, L19809, doi:10.1029/2007GL030021.

Hong, S.-Y., Y. Noh, and J. Dudhia (2006), A new vertical diffusion package with an explicit treatment of entrainment processes, *Mon. Weather Rev.*, *134*, 2318–2341, doi:10.1175/MWR3199.1.

Kondo, Y., et al. (2006), Temporal variations of elemental carbon in Tokyo, *J. Geophys. Res.*, *111*, D12205, doi:10.1029/2005JD006257.

Kondo, Y., et al. (2008), Formation and transport of oxidized reactive nitrogen, ozone, and secondary organic aerosol in Tokyo, *J. Geophys. Res.*, *113*, D21310, doi:10.1029/2008JD010134.

Li, C., L. T. Marufu, R. R. Dickerson, Z. Li, T. Wen, Y. Wang, P. Wang, H. Chen, and J. W. Stehr (2007), In situ measurements of trace gases and aerosol optical properties at a rural site in northern China during East Asian Study of Tropospheric Aerosols: An International Regional Experiment 2005, *J. Geophys. Res.*, *112*, D22S04, doi:10.1029/2006JD007592.

Malm, W. C., J. F. Sisler, D. Huffman, R. A. Eldred, and T. A. Cahill (1994), Spatial and seasonal trends in particle concentrations and optical extinction in the United States, *J. Geophys. Res.*, *99*, 1347–1370, doi:10.1029/93JD02916.

Malm, W. C., et al. (2005), Intercomparison and closure calculations using measurements of aerosol species and optical properties during the Yosemite Aerosol Characterization Study, *J. Geophys. Res.*, *110*, D14302, doi:10.1029/2004JD005494.

Matsui, H., M. Koike, N. Takegawa, Y. Kondo, R. J. Griffin, M. Miyazaki, Y. Yokouchi, and T. Ohara (2009), Secondary organic aerosol formation in urban air: Temporal variations and possible contributions from unidentified hydrocarbons, *J. Geophys. Res.*, *114*, D04201, doi:10.1029/2008JD010164.

McKeen, S., et al. (2005), Assessment of an ensemble of seven real-time ozone forecasts over eastern North America during the summer of 2004, *J. Geophys. Res.*, *110*, D21307, doi:10.1029/2005JD005858.

McKeen, S., et al. (2007), Evaluation of several PM2.5 forecast models using data collected during the ICARTT/NEAQS 2004 field study, *J. Geophys. Res.*, *112*, D10S20, doi:10.1029/2006JD007608.

Nenes, A., S. N. Pandis, and C. Pilinis (1998), ISORROPIA: A new thermodynamic equilibrium model for multiphase multicomponent inorganic aerosols, *Aquat. Geochem.*, *4*, 123–152, doi:10.1023/A:1009604003981.

Odum, J. R., T. Hoffmann, F. Bowman, D. Collins, R. C. Flagan, and J. H. Seinfeld (1996), Gas/particle partitioning and secondary organic aerosol yields, *Environ. Sci. Technol.*, *30*, 2580–2585, doi:10.1021/es950943+.

Remer, L. A., et al. (2005), The MODIS aerosol algorithm, products, and validation, *J. Atmos. Sci.*, *62*, 947–973, doi:10.1175/JAS3385.1.

Roy, B., R. Mathur, A. B. Gilliland, and S. Howard (2007), A comparison of CMAQ-based aerosol properties with IMPROVE, MODIS, and AERONET data, *J. Geophys. Res.*, *112*, D14301, doi:10.1029/2006JD008085.

Skamarock, W. C., J. B. Klemp, J. Dudhia, D. O. Gill, D. M. Barker, W. Wang, and J. G. Powers (2005), A description of the advanced research WRF version 2, Tech. Note NCAR/TN-468+STR, Natl. Cent. Atmos. Res., Boulder, Colo.

Streets, D. G., et al. (2003), An inventory of gaseous and primary aerosol emissions in Asia in the year 2000, *J. Geophys. Res.*, *108*(D21), 8809, doi:10.1029/2002JD003093.

Streets, D. G., Q. Zhang, L. Wang, K. He, J. Hao, Y. Wu, Y. Tang, and G. R. Carmichael (2006), Revisiting China's CO emissions after the Transport and Chemical Evolution over the Pacific (TRACE-P) mission: Synthesis of inventories, atmospheric modeling, and observations, *J. Geophys. Res.*, *111*, D14306, doi:10.1029/2006JD007118.

Streets, D. G., et al. (2007), Air quality during the 2008 Beijing Olympic Games, *Atmos. Environ.*, *41*, 480–492, doi:10.1016/j.atmosenv.2006.08.046.

Takegawa, N., T. Miyakawa, Y. Kondo, J. L. Jimenez, Q. Zhang, D. R. Worsnop, and M. Fukuda (2006), Seasonal and diurnal variations of submicron organic aerosols in Tokyo observed using the Aerodyne aerosol mass spectrometer, *J. Geophys. Res.*, *111*, D11206, doi:10.1029/2005JD006515.

Takegawa, N., et al. (2009a), Performance of an Aerodyne aerosol mass spectrometer (AMS) during intensive campaigns in China in the summer of 2006, *Aerosol Sci. Technol.*, *43*, 189–204, doi:10.1080/02786820802582251.

Takegawa, N., et al. (2009b), Variability of submicron aerosol observed at a rural site in Beijing in the summer of 2006, *J. Geophys. Res.*, *114*, D00G05, doi:10.1029/2008JD010857.

Turpin, B. J., and J. J. Huntzicker (1995), Identification of secondary organic aerosol episodes and quantification of primary and secondary organic aerosol concentration during SCAQS, *Atmos. Environ.*, *29*, 3527–3544, doi:10.1016/1352-2310(94)00276-Q.

Volkamer, R., J. L. Jimenez, F. San Martini, K. Dzepina, Q. Zhang, D. Salcedo, L. T. Molina, D. R. Worsnop, and M. J. Molina (2006), Secondary organic aerosol formation from anthropogenic air pollution: Rapid and higher than expected, *Geophys. Res. Lett.*, *33*, L17811, doi:10.1029/2006GL026899.

Wild, O., X. Zhu, and M. J. Prather (2000), Fast-J: Accurate simulation of in- and below-cloud photolysis in tropospheric chemical models, *J. Atmos. Chem.*, *37*, 245–282, doi:10.1023/A:1006415919030.

World Health Organization (2006), Air Quality Guidelines: Global Update 2005: Particulate Matter, Ozone, Nitrogen Dioxide, and Sulfur Dioxide, Copenhagen.

Zaveri, R. A., and L. K. Peters (1999), A new lumped structure photochemical mechanism for large-scale applications, *J. Geophys. Res.*, *104*, 30,387–30,415, doi:10.1029/1999JD900876.

Zaveri, R. A., R. C. Easter, and A. S. Wexler (2005a), A new method for multicomponent activity coefficients of electrolytes in aqueous atmospheric aerosols, *J. Geophys. Res.*, *110*, D02201, doi:10.1029/2004JD004681.

Zaveri, R. A., R. C. Easter, and L. K. Peters (2005b), A computationally efficient Multicomponent Equilibrium Solver for Aerosols (MESA), *J. Geophys. Res.*, *110*, D24203, doi:10.1029/2004JD005618.

Zaveri, R. A., R. C. Easter, J. D. Fast, and L. K. Peters (2008), Model for Simulating Aerosol Interactions and Chemistry (MOSAIC), *J. Geophys. Res.*, *113*, D13204, doi:10.1029/2007JD008782.

Zhang, Q., M. R. Alfarra, D. R. Worsnop, J. D. Allan, H. Coe, M. R. Canagaratna, and J. L. Jimenez (2005), Deconvolution and quantification of hydrocarbon-like and oxygenated organic aerosols based on aerosol mass spectrometry, *Environ. Sci. Technol.*, *39*, 4938–4952, doi:10.1021/es048568l.

Zhang, Q., D. G. Streets, K. He, and Z. Klimont (2007), Major components of China's anthropogenic primary particulate emission, *Environ. Res. Lett.*, *2*, 045027, doi:10.1088/1748-9326/2/4/045027.

Zhang, Q., et al. (2009), Asian emissions in 2006 for the NASA INTEX-B mission, *Atmos. Chem. Phys.*, *9*, 5131–5153.

Zhang, Y., P. Liu, B. Pun, and C. Seigneur (2006), A comprehensive performance evaluation of MM5-CMAQ for the summer 1999 southern oxidants study episode, part III: Diagnostic and mechanistic evaluations, *Atmos. Environ.*, *40*, 4856–4873, doi:10.1016/j.atmosenv.2005.12.046.

D. R. Blake, Department of Chemistry, University of California, Irvine, CA 92697-2025, USA. (drblake@uci.edu)

S.-Y. Chang, Department of Public Health, Chung Shan Medical University, Taichung City 40201, Taiwan. (sychang@csmu.edu.tw)

J. D. Fast and R. A. Zaveri, Atmospheric Science and Global Change Division, Pacific Northwest National Laboratory, MSINK9-30, P.O. Box 999, Richland, WA 99352, USA. (jerome.fast@pnl.gov; rahul.zaveri@pnl.gov)

M. Hu and T. Zhu, State Key Laboratory of Environmental Simulation and Pollution Control, College of Environmental Sciences and Engineering, Peking University, Beijing 100871, China. (minhu@pku.edu.cn; tzhu@pku.edu.cn)

K. Kita, Department of Environmental Science, Graduate School of Science, Ibaraki University, Bunkyo 2-1-1, Mito, Ibaraki, 310-8512, Japan. (kita@mx.ibaraki.ac.jp)

M. Koike, Department of Earth and Planetary Science, Graduate School of Science, University of Tokyo, Hongo 7-3-1, Bunkyo-ku, Tokyo, 113-0033, Japan. (koike@eps.s.u-tokyo.ac.jp)

Y. Kondo, H. Matsui, and N. Takegawa, Research Center for Advanced Science and Technology, University of Tokyo, 4-6-1 Komaba, Meguro, Tokyo 153-8904, Japan. (y.kondo@atmos.rcast.u-tokyo.ac.jp; matsui@atmos.rcast.u-tokyo.ac.jp; takegawa@atmos.rcast.u-tokyo.ac.jp)

Y. Miyazaki, Institute of Low Temperature Science, Hokkaido University, Kita-19, Nishi-8, Kita-ku, Sapporo 060-0819, Japan. (yuzom@pop.lowtem.hokudai.ac.jp)

D. G. Streets and Q. Zhang, Decision and Information Sciences Division, Argonne National Laboratory, Argonne, IL 60439-4803, USA. (dstreets@anl.gov; zhangq@anl.gov)